

Restoring calcium crosstalk between ER and mitochondria promotes intestinal stem cell rejuvenation through autophagy in aged *Drosophila*

Received: 23 August 2024

Accepted: 15 May 2025

Published online: 27 May 2025

 Check for updatesYao Zhang , Peng Ma , Saifei Wang , Shuxin Chen  & Hansong Deng  

Breakdown of calcium network is closely associated with cellular aging. Previously, we found that cytosolic calcium (CytoCa^{2+}) levels were elevated while mitochondrial calcium (MitoCa^{2+}) levels were decreased and associated with metabolic shift in aged intestinal stem cells (ISCs) of *Drosophila*. How MitoCa^{2+} was decoupled from the intracellular calcium network and whether the reduction of MitoCa^{2+} drives ISC aging, however, remains unresolved. Here, we show that genetically restoring MitoCa^{2+} can reverse ISC functional decline and promote intestinal homeostasis by activating autophagy in aged flies. Further studies indicate that MitoCa^{2+} and Mitochondria–ER contacts (MERCs) form a positive feedback loop via *IP3R* to regulate autophagy independent of *AMPK*. Breakdown of this loop is responsible for MitoCa^{2+} reduction and ISC dysfunction in aged flies. Our results identify a regulatory module for autophagy initiation involving calcium crosstalk between the ER and mitochondria, providing a strategy to treat aging and age-related diseases.

The functional decline of stem cell activities in many tissues is a hallmark of aging. Intestinal stem cells (ISCs) are the only cell type capable of dividing in response to the physiological demands in the adult fly gut^{1,2}. As in mammals, epithelial turnover in the *Drosophila* intestine is also maintained by ISCs. During homeostasis, ISCs are mostly quiescent but can initiate a proliferative response to stress conditions such as infection, toxins as well as aging³. During aging, the intestinal epithelium undergoes dysplasia, which is characterized by ISC overproliferation and mis-differentiation, where ISCs show mixed feature with the enteroblast (EB), the daughter cell^{4,5}.

Calcium is a versatile second messenger that is critical in regulating fundamental physiological functions. The concentration of Ca^{2+} varies between different subcellular compartments, which are established and maintained by Ca^{2+} channels and pumps^{6,7}. The ER is the largest intracellular calcium store and Ca^{2+} homeostasis in ER is achieved by channels that release Ca^{2+} from the ER lumen into the cytosol - including *IP3Rs* and *RyRs* - and mechanisms that return Ca^{2+} to

the ER, such as *SERCA* pumps and store-operated Ca^{2+} entry (*SOCE*)^{7,8}. ER releases Ca^{2+} via *IP3R* and allows Ca^{2+} to passively enter the mitochondrial outer membrane (OMM) via *VDAC1*, a high conductance protein⁹. However, the inner mitochondrial membrane (IMM) is impermeable to Ca^{2+} , and Ca^{2+} enters through the mitochondrial calcium uniporter (*MCU*) complex, which consists of the inner membrane channel *MCU* and regulatory subunits including *MICU1* and *EMRE*^{10,11}. High Ca^{2+} concentrations at the mitochondrial intermembrane space activate *MCU* to mediate the entry of Ca^{2+} into the mitochondrial matrix, where Ca^{2+} stimulates the activities of tricarboxylic acid (TCA) cycle, β -oxidation and respiratory complexes to enhance ATP generation¹².

AMPK (AMP-activated protein kinase) is a cellular energy sensor that activated by falling energy status^{13,14}. In mammalian cell lines, reduction of MitoCa^{2+} by disruption of MERCs or by the Ca^{2+} chelator BAPTA-AM induced a bioenergetic crisis and activates *AMPK*-mediated (macro)autophagy to cope with energy depletion^{15–17}. Recently, we and

Yangzhi Rehabilitation Hospital, Sunshine Rehabilitation Center, Frontier Science Center for Stem Cell Research, School of Life Sciences and Technology, Tongji University, Shanghai 20092, China. ✉e-mail: hdeng@tongji.edu.cn

others found that subcellular calcium level in cytosol (CytoCa²⁺) and mitochondria serves as critical coordinators during the transition of ISCs from quiescence to proliferation^{8,18,19}. This adaption failed in old ISCs, which have sustained higher CytoCa²⁺ and lack efficient MitoCa²⁺ uptake and have undergone a Warburg-like metabolic switch involving increased lactate production and reduced ATP levels, contributing to their deregulated proliferative activity^{8,18}. How MitoCa²⁺ was reduced and whether restoring MitoCa²⁺ can reverse the metabolic profile and age-related defects in ISCs remains largely unknown.

The MERCs, also known as mitochondria-associated membranes (MAMs), are the physical links between the ER and mitochondria, providing an interface for Ca²⁺ transfer^{9,20}. These structures are dynamic and highly heterogeneous among tissues and species²¹. MERCs establishment is regulated by multiple scaffold and tethering factors that include among others *MFN2*, *IP3Rs-GRP75-VDACs*, *FIS1-BAP31*, *VAPB-PTPIP51*, *Mmm1*, and *SIGMAR1*^{22,23}. Increasing evidence indicated that MERC is one of the membrane sources for autophagosomes and is the initiation site for autophagy²⁴. In multicellular organisms, the *Atg1* complex (including *ATG1*, *FIP200*, *Atg17* and *Atg13*) is targeted to the ER and recruits the class III (*PI(3)P*) kinase complex (including *ATG6* and *ATG14*) for initiation and maturation of pre-autophagosomes upon autophagy induction^{25,26}. For instance, the omegasome marker *DFCP1/ZFYVE1* (double FYVE domain-containing protein 1) and *ATG14* was recruited to the MERCs during starvation²⁷. When MERCs were disrupted by *MFN2* knockdown, *ATG14* is no longer localized in the MERCs and the autophagosome formation is also inhibited²⁸, suggesting that MERCs play an indispensable role for autophagosome formation. A recent study has also shown that *IP3R* mediated Ca²⁺ transients at the outer surface of the ER triggers autophagosome initiation by promoting the formation of fluid-like *FIP200* puncta²⁹. Whether the calcium oscillations generated between the ER and the cytosol, or between the ER and mitochondria via MERCs, are responsible for the initiation of autophagy, and how the oscillations are generated and maintained, remains unclear.

Accumulating evidence indicates that autophagy declines with age and that impaired autophagy is associated with stem cell aging³⁰. In mice, the regenerative capacity of muscle stem cells is maintained by basal autophagy, and its deregulation leads to premature entry into an irreversible senescent state³¹. Similarly, autophagy genes such as *Atg5* and *Atg7* are necessary for ISC maintenance and gut homeostasis³². In *Drosophila*, autophagy deficient ISCs show elevated DNA damage and cell cycle arrest during aging and lead to unlimited ISC proliferation or apoptosis^{33,34}. These results reveal the crucial role of autophagy in preserving proper stem cell function for the continuous renewal of the intestinal epithelium. Indeed, activation of *AMPK* is linked to improved intestinal homeostasis during aging and extended lifespan in *Drosophila*³⁵. How autophagy was impaired during aging was largely unknown.

Here, we found that MitoCa²⁺ influx retrogradely activates *IP3R* in MERCs, generating Ca²⁺ oscillations in MERCs that promote autophagy independent of *AMPK*. Genetic restoration of mitoCa²⁺ levels re-establishes the MitoCa²⁺-*IP3R*-MERCs feedback loop and delays ISC aging by autophagy.

Results

Deficient MitoCa²⁺ uptake contributes to ISC dysfunction in aged *Drosophila*

Our previous results showed that MitoCa²⁺ was reduced in aged ISCs, while CytoCa²⁺ remained higher^{8,18}. To further trace intracellular calcium pattern in ISCs during aging, genetically encoded calcium reporters targeted to mitochondria (UAS::MitoGCaMP3) or cytosol (UAS::GCaMP5) were expressed specifically in ISCs by combining *esg::Gal4^{TS}* with *Su(H)::Gal80* (ISC-Gal4^{TS}). In ex vivo live-imaged midguts, CytoCa²⁺ level exhibited a progressive increase from around 30 days of age, whereas MitoCa²⁺ level decreased gradually (Fig. 1a and

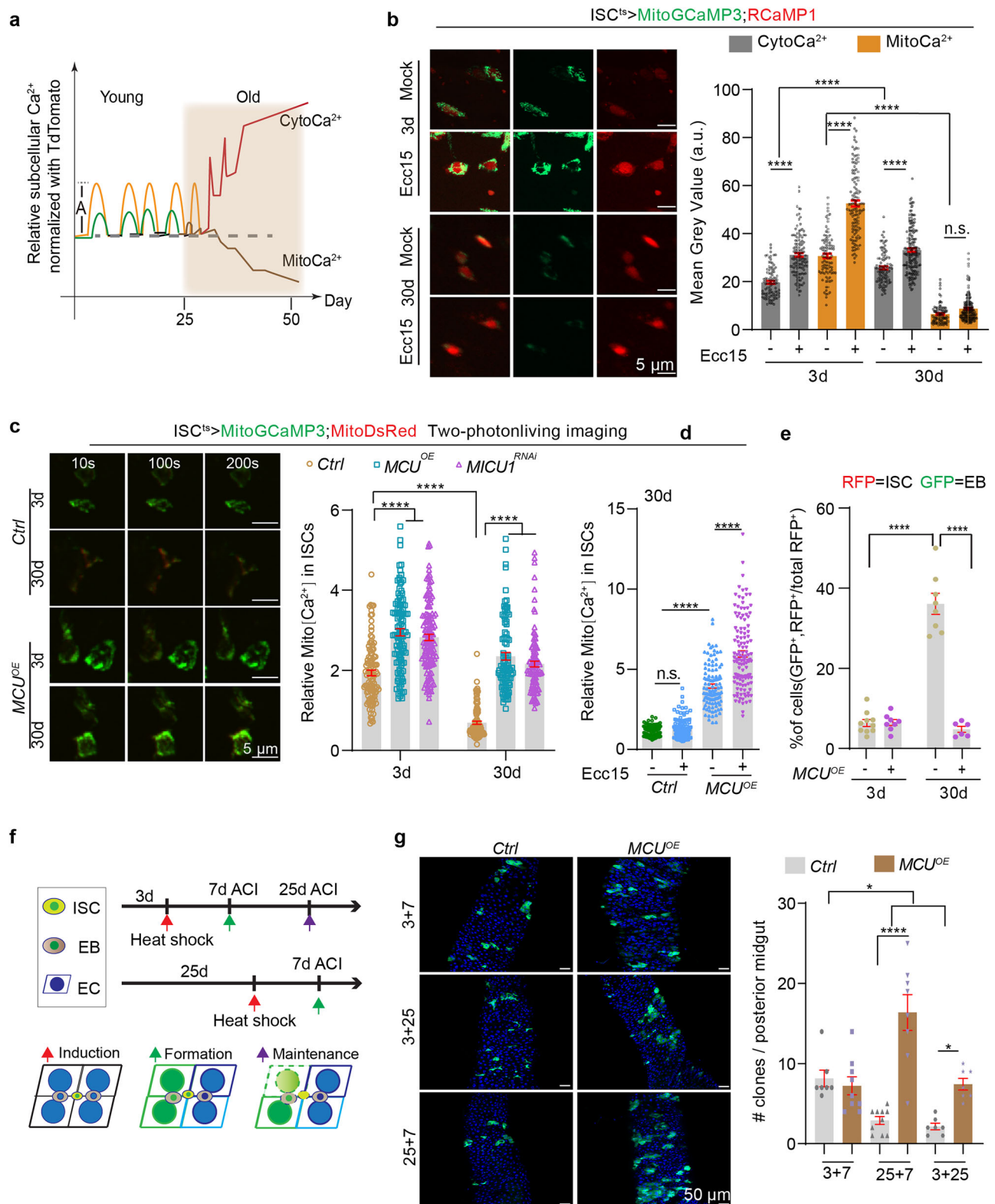
Supplementary Fig. 1a, b), implied that the breakdown of Ca²⁺ homeostasis started at middle age (The lifespan of flies under conventional conditions is estimated to be 60–70 days³⁶). The simultaneous monitoring of CytoCa²⁺ and MitoCa²⁺ in individual ISCs (UAS::MitoGCaMP3 for mitochondria, UAS::RCaMP1 for cytosol) revealed that both CytoCa²⁺ and MitoCa²⁺ in ISCs from young animals (3 d old) were significantly increased upon infection using *Erwinia carotovora carotovora 15* (*Ecc15*), a mild enteropathogen that induces a transient proliferative response in the gut epithelium³⁷. In contrast, in ISCs from aged animals (30 d old), CytoCa²⁺ levels were further increased by infection, but MitoCa²⁺ levels remained lower than those in young animals (Fig. 1b). This suggested that the MitoCa²⁺ response to external stimuli is impaired in aged ISCs.

The components of mitochondrial calcium uniporter (MCU) complex are conserved in *Drosophila*, such as the pore-forming *MCU* (CG18769) and the negative gatekeeper *MICU1* (CG4495)^{38,39}. The ISC specific overexpression of *MCU* (*MCU^{OE}*) or the knockdown of *MICU1* (*MICU1^{RNAi}*) was sufficient to increase MitoCa²⁺ in young ISCs and also to restore MitoCa²⁺ in old ones (Fig. 1c and Supplementary Movie 1–6). Conversely, the overexpression of *MICU1* (*MICU1^{OE}*) or the knockdown of *MCU* (*MCU^{RNAi}*) was sufficient to decrease MitoCa²⁺ in young ISCs (Supplementary Fig. 1c and Supplementary Movie 7, 8). Notably, *MCU* overexpression also resulted in a reduction in elevated CytoCa²⁺ in aged ISCs (Supplementary Fig. 1a). Furthermore, *MCU* overexpression was sufficient to restore MitoCa²⁺ levels, which were reduced and insensitive to *Ecc15* infection in aged ISCs (Fig. 1d and Supplementary Fig. 1d). These results suggested that MitoCa²⁺ levels in ISCs are controlled by the MCU complex.

We then examined whether genetically restoring MitoCa²⁺ was sufficient to rescue aged ISCs dysfunction. NRE-eGFP is a genetic reporter of Notch signaling⁴⁰, which expressed exclusively in enteroblast cells (EB), while the percentage of NRE-eGFP positive ISCs significantly increased in aged midguts, indicating that the aged ISCs underwent mis-differentiation and displayed mixed feature of ISC and EB cells⁴, which can be restored by *MCU^{OE}* (Fig. 1e and Supplementary Fig. 1e). Mosaic analysis with a repressible cell marker (MARCM) is a positive mosaic labeling system that has been widely used to study the self-renewal and differentiation abilities of ISCs in *Drosophila*^{1,2,41}. Two different strategies were exploited to monitor ISC activity: clones were induced in young animals (3 d) and the clone number was checked 7 days (3 + 7) or 25 days (3 + 25) after clone induction (ACI), reflecting the ability of ISCs pool to form and maintain these clones. Alternatively, clones were induced in aged animals (25 d) and then checked 7 days ACI to check the clone forming ability of aged ISCs (Fig. 1f). Intriguingly, both the clone formation and maintenance capacity of ISC declined in aged animals, and which can be restored by *MCU^{OE}* (Fig. 1g). Taken together, these results indicated that old ISCs lack efficient MitoCa²⁺ uptake and the dysfunctions in aged ISCs can be improved by restoring MitoCa²⁺ levels.

Restoration of MitoCa²⁺ delays ISC aging and promotes intestinal homeostasis in aged flies

We then examined the role of MitoCa²⁺ in ISC aging and intestinal function. Cell cycle indicated by the *FUCCI* system (fluorescent ubiquitination-based cell cycle indicator)⁴² showed that the ratio of ISCs in G1 vs in G2/M stage was significantly increased in aged ISCs, indicating cell cycle dysregulation (Fig. 2a and Supplementary Fig. 2a). Consistent with previous studies^{18,34}, lactate level (indicated by Laconic, a FRET based Lactate reporter) and DNA damages (indicated by gamma-H2AX staining) were increased in aged ISCs (Fig. 2b and Supplementary Fig. 2b, c). Intriguingly, cell cycle dysregulation, lactate level as well as gamma-H2AX accumulation were all restored in aged ISCs with *MCU^{OE}* or *MICU1^{RNAi}* by the TARGET system⁴³ (Fig. 2a–c and Supplementary Fig. 2b–d) and also by a drug (RU486) inducible ISC/EB specific driver 5961::GS⁴⁴ (Supplementary Fig. 2e). Conversely, fewer number and



reduced clone size (cell number within the clone) were observed in *MICU1^{OE}* (Supplementary Fig. 3a). Moreover, the knockdown of *MCU* in young ISCs (10 d) exhibited similarities to aged ISCs, including cell cycle dysregulation and DNA damage accumulations (Supplementary Fig. 3b, c). Age-related ISC dysfunction impairs midgut digestive functions, such as the loss of gut acid-base homeostasis and the decline of food intake and excretion^{45,46}. Intriguingly, ISC-specific overexpression of *MCU* was sufficient to restore the deterioration of

gut pH homeostasis (Fig. 2d) and mitigated the decrease of food intake (Fig. 2e) and excretion (Fig. 2f) in aged guts. Together, these results indicated that restoring MitoCa²⁺ levels is sufficient to delay ISC aging and restore gut homeostasis in *Drosophila*.

Autophagy is activated by MitoCa²⁺ to delay ISC aging

MitoCa²⁺ level is essential for bioenergetics and our previous results showed that ATP level was reduced in aged ISCs¹⁸. Severe ATP

Fig. 1 | Deficient MitoCa²⁺ uptake contributes to ISC dysfunction in aged *Drosophila*. **a** Plot summary of calcium level in cytosol and mitochondria at different time points. **A**, amplitude. **b** Representative images and quantification of MitoCa²⁺ (green) and CytoCa²⁺ (red) in ISCs of young (3 d) and old animals (30 d) with indicated genotypes exposed or not to *Ecc15* infection. Data show mean \pm S.E.M ($n = 95, 122, 99$ and 173 cells, from left to right) based on two-way ANOVA with Tukey's multiple comparison test. **** $P < 0.0001$. Scale bar, $5 \mu\text{m}$. **c** Representative images and quantification of relative MitoCa²⁺ levels in ISCs of young (3 d) or old animals (30 d) with indicated genotypes. MitoGCaMP3 (green), MitoDsRed (red). Data show mean \pm S.E.M ($n = 109, 110, 131, 104, 93$ and 104 cells, from left to right) based on two-way ANOVA with Tukey's multiple comparison test. **** $P < 0.0001$. Scale bar, $5 \mu\text{m}$. **d** Quantification of relative MitoCa²⁺ levels in aged ISCs (30 d) with indicated genotypes exposed or not to *Ecc15* infection. Data show mean \pm S.E.M ($n = 133, 129, 108$ and 126 cells, from left to right) based on two-way ANOVA with Tukey's multiple

comparison test. **** $P < 0.0001$. **e** Quantification of the number of mis-differentiation ISCs with indicated genotypes at different ages. Data show mean \pm S.E.M ($n = 10, 8, 8$ and 6 guts, from left to right) based on two-way ANOVA with Tukey's multiple comparison test. **** $P < 0.0001$. **f** Schematics for MARCM clone analysis. Main cell types (upper left), clonal formation (clone of GFP positive cells) and clonal maintenance (shedding GFP positive cells in the clone) (bottom) were shown as schematics. **g** Representative images and quantification of clone numbers in the posterior midgut with indicated genotypes at different ages. ISC clones (green) and nuclei (blue). Data show mean \pm S.E.M ($n = 7, 9, 10, 8, 7$ and 7 guts, from left to right) based on two-way ANOVA with Tukey's multiple comparison test. * $P < 0.05$ and **** $P < 0.0001$. Scale bar: $50 \mu\text{m}$. Each experiment was repeated for 3 times (**b–e, g**). See Supplementary Table 1 for genotypes. Source data are provided as a Source Data file.

depletion could lead to cell apoptosis or necrosis⁴⁷. Previous studies have shown that genetic inhibition of β -oxidation leads to ISC necrosis⁴⁸. Neutral lipid content (stained by LipidTOX) was largely unchanged by genetically inhibiting MitoCa²⁺ level in quiescent ISCs as well as in active ISCs upon infection (Supplementary Fig. 4a). The percentage of apoptotic (indicated by Cleaved Caspase-3 staining) or necrotic ISCs (indicated by Propidium iodide (PI) staining) was also largely unchanged in *MCU^{OE}* or *MICU1^{RNAi}* in aged ISCs (Supplementary Fig. 4b, c). We then tested whether MitoCa²⁺ delay ISC aging by regulating autophagy. Indeed, the number of autophagosomes (mCherry-Atg8 positive puncta) and acidic lysosomes (Lysotracker positive staining) in ISCs were significantly increased by *MCU^{OE}* or by *MICU1^{RNAi}* (Fig. 3a, b and Supplementary Fig. 5a, b). The mCherry-Atg8 positive vesicles in *MCU^{OE}* ISCs readily colocalized with the lysosome (indicated by GFP-Lamp1), implied that these autophagosomes were readily fused with lysosome (Supplementary Fig. 5c). Lysosomal activity can be assessed using two fluorescent dye indicators: Magic Red Cathepsin B (Magic Red) and DQ-BSA^{49,50}. More puncta of Magic Red and DQ-BSA were observed in ISCs by *MCU^{OE}* (Fig. 3c, d and Supplementary Fig. 5d, e).

Further track the autophagic flux by the tandem GFP-mCherry-Atg8a reporter in which GFP is rapidly quenched in an acidic environment⁵¹, showed that the percentage of autolysosomes (mCherry⁺/GFP⁺, red puncta) was significantly increased in *MCU^{OE}* ISCs (Fig. 3e and Supplementary Fig. 5f). Consistently, accumulation of autophagosomes (mCherry⁺/GFP⁺, yellow puncta) were also increased in *MCU^{OE}* ISCs under Chloroquine (CQ, an inhibitor of autophagosome-lysosome fusion⁵²) treatment (Fig. 3f and Supplementary Fig. 5g). On the other hand, both of the increased mCherry-ATG8a- and Lysotracker-positive puncta induced by starvation were reduced in *MCU^{RNAi}* or *MICU1^{OE}* ISCs (Fig. 3g, h and Supplementary Fig. 5h, i). Furthermore, although these autophagosomes can readily colocalize with GFP-Lamp1 (Supplementary Fig. 5c), GFP signals of GFP-mCherry-Atg8a were retained in *MICU1^{OE}* ISCs (Supplementary Fig. 5f). *Ref(2)P* is the ortholog of *P62* in *Drosophila*, which is a conserved autophagy substrate^{53,54}. The number of *Ref(2)P*-GFP puncta in ISCs was significantly reduced by *MCU^{OE}*, whereas it was increased by *MICU1^{OE}* (Fig. 3i and Supplementary Fig. 5j). Transmission electron microscope (TEM) images also indicated that the number of autophagosomes and/or autolysosomes in ISCs was significantly increased by *MCU^{OE}* or *MICU1^{RNAi}* (Fig. 3j and Supplementary Fig. 5k). These data indicated that autophagic activity was sensitive to MitoCa²⁺ in ISCs of fly intestine. In addition, overexpression of *MCU* in indirect flight muscles by IFM::Gal4 also promoted autophagy (indicated by increased mCherryAtg8+ puncta) in muscles (Supplementary Fig. 6a). Treatment of CQ can completely block *MCU^{OE}* induced ISC rejuvenation on the number of clones induced in old age (25 + 7) or maintenance of clones induced at young age (3 + 25) (Fig. 3k and Supplementary Fig. 6b). DNA damage suppressed by *MICU1^{RNAi}* in aged ISCs was blocked when autophagy was disrupted by *Atg1^{RNAi}* (Fig. 3l and Supplementary Fig. 6c). On the

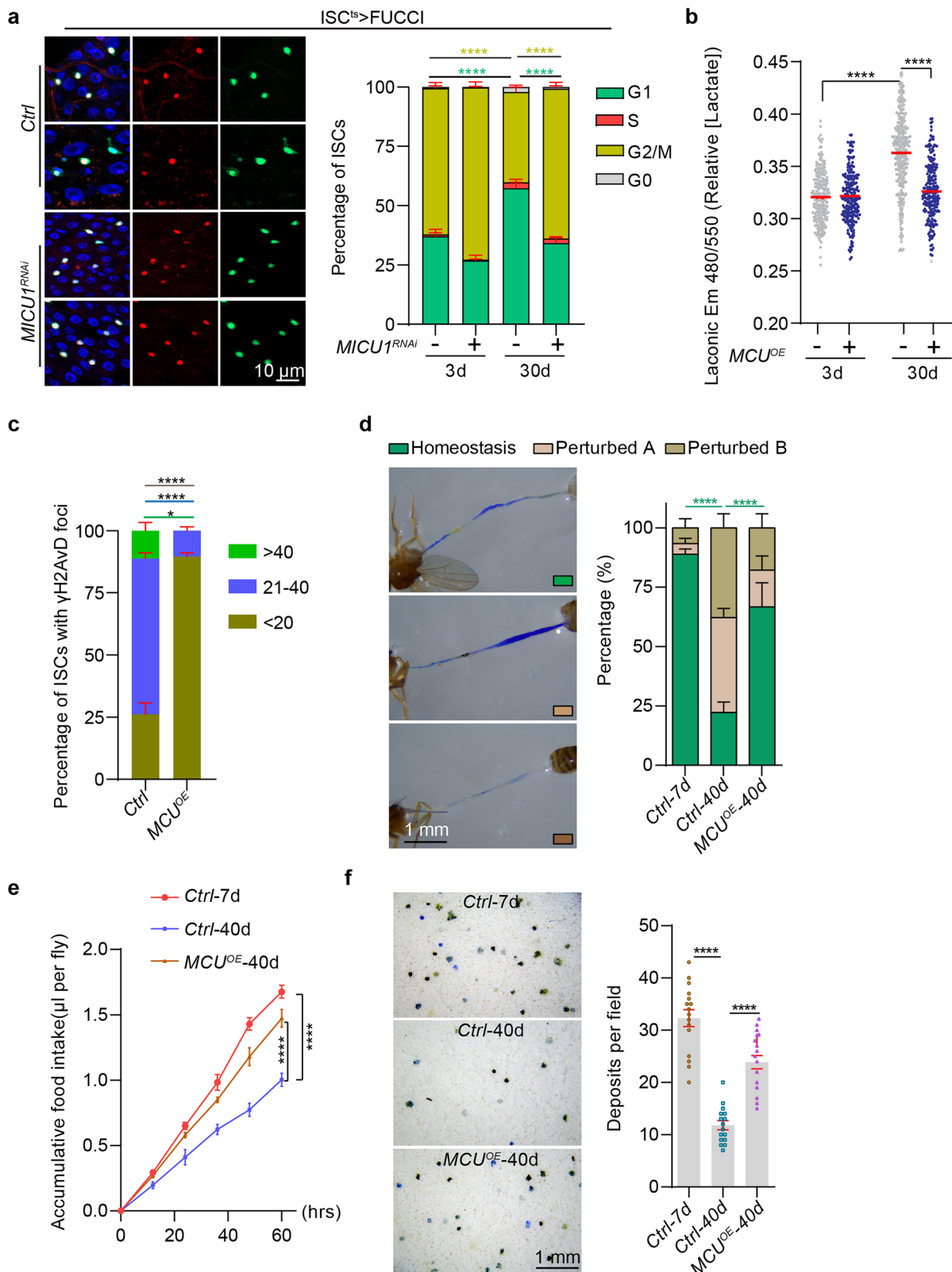
other hand, increasing autophagy by ISC specific *Atg17* overexpression, a component in the *ATG1* complex essential for phagophore formation⁵⁵, was sufficient to suppress DNA damages in aged ISCs (Fig. 3m and Supplementary Fig. 6d–f). Together, these results indicated that MitoCa²⁺-mediated anti-aging effect is dependent on autophagy.

MitoCa²⁺ promotes autophagy by activating *IP3R*-mediated Ca²⁺ release from the ER

We then attempted to elucidate the mechanism by which MitoCa²⁺ stimulates autophagy. Autophagosome initiation in ISCs, as indicated by antibody staining against endogenous Atg8a^{56,57} (Fig. 4a), as well as by genetic reporters for *Atg13* in the *Atg1* complex, *Atg6* in the *PI(3)P* kinase complex, *Atg9* for autophagosome membrane source⁵⁸ and *ZFYVE1* in omegasomes, was robustly increased by *MCU^{OE}* (Fig. 4b and Supplementary Fig. 7a–d). Endocytosis (indicated by the levels of *Rab5* and *Rab7*, markers for early and late endosomes respectively), was mostly unaffected by *MCU^{OE}* in ISCs (Supplementary Fig. 7e–g). *AMPK* is a central regulator of autophagy¹³. However, *AMPK* activity, indicated by *AMPK*-SPARK (a phase separation dependent genetic reporter of *AMPK* activity)⁵⁹ and downstream *mTOR* activity (shown by phospho-4EBP staining) was largely normal in *MCU^{OE}* ISCs (Supplementary Fig. 8a, b). Consistently, the cell size of ISCs was largely unchanged by genetically regulating MitoCa²⁺ levels (Supplementary Fig. 8c). Meanwhile, although autophagic activity in ISCs (indicated by immunostaining against endogenous p62⁶⁰) was found to be both sensitive to *AMPK* and MitoCa²⁺ levels, epistatic analysis indicated that the inhibition of *AMPK* activities suppresses autophagy mediated by MitoCa²⁺, and vice versa (Supplementary Fig. 8d). Excessive ROS level can activate autophagy through JNK(c-Jun N-Terminal Kinase)⁶¹. However, no obvious increase of mitochondrial ROS (H₂O₂) level (shown by a genetic ROS sensor MitoRoGFP2-Orp1¹⁸), while *JNK* activity (indicated by TRE-RFP⁶²) was even reduced by *MCU^{OE}* in ISCs (Supplementary Figs. 8e, f).

IP3R, instead of *RyR*, is the main calcium release channel in the ER of *Drosophila* ISCs^{7,8} and *Itpr* encodes the sole homolog of *IP3R* in fly genome⁶³. MitoCa²⁺ in ISCs was inhibited by *Itpr* knockdown (*Itpr^{RNAi}*), whereas increased by *Itpr* overexpression (*Itpr^{OE}*) (Fig. 4c and Supplementary Fig. 9a), indicating that MitoCa²⁺ level was coupled with *IP3R*-mediated Ca²⁺ release from the ER.

Since *IP3R* was shown to trigger Ca²⁺ oscillations on the ER outer membrane and induce autophagosome biogenesis²⁹, we then explore whether MitoCa²⁺ can promote autophagy by eliciting Ca²⁺ oscillations on the ER outer membrane (Fig. 4d). ER-GCaMP6-210, a sensitive reporter of Ca²⁺ in the ER lumen (ERCa²⁺)⁶⁴, was utilized to reflect the activity of *IP3R*. Surprisingly, increasing MitoCa²⁺ in ISCs by *MICU1^{RNAi}* was sufficient to decrease ERCa²⁺ levels, which was blocked when *Itpr* was simultaneously silenced, indicating that increasing MitoCa²⁺ promoted Ca²⁺ release from the ER matrix by activating *IP3R* (Fig. 4e). Meanwhile, we generated an *Itpr*-HA knock-in transgene by CRISPR-



Cas9 mediated homologous recombination (Supplementary Fig. 10a) to test whether its protein level or subcellular localization were altered by MitoCa²⁺ level. Indeed, *Itpr*-positive signals (indicated by anti-HA staining) form obvious puncta which are closely associated with KDEL-GFP (Supplementary Fig. 10b) in ISCs. Intriguingly, these puncta were significantly increased by *MCU*^{OE} in ISCs, further indicated that MitoCa²⁺ promotes *IP3R* activity (Supplementary Fig. 10c). Autophagy

induced by starvation or *MCU*^{RNAi} in ISCs (quantified by the number of autophagosomes and Lysotracker) was also diminished by *Itpr*^{RNAi} (Fig. 4f, g and Supplementary Fig. 9b–g), while overexpressing *Itpr* promoted ISCs autophagic activity (Fig. 4h and Supplementary Fig. 11a, b). On the other hand, DNA damage in aged ISCs suppressed by *MCU*^{RNAi} was blocked by *Itpr*^{RNAi} (Fig. 4i and Supplementary Fig. 11c), and *Itpr*^{OE} was sufficient to suppress DNA damage in aged ISCs (Fig. 4j

Fig. 2 | Restoration of MitoCa²⁺ delays ISC aging and promotes intestinal homeostasis in aged flies. **a** Representative images and quantification of cell cycle stages (shown by different color) of ISCs with indicated genotypes at different ages by the *Fucci* system. ISCs (green and/or red) and nuclei (blue). Data show mean \pm S.E.M ($n = 858, 1504, 978$ and 1100 cells, from left to right) based on two-way ANOVA with Tukey's multiple comparison test. **** $P < 0.0001$. Scale bar, $10\ \mu\text{m}$. **b** Quantification of relative lactate levels (Em 480/550 fluorescence ratios) in ISCs with indicated genotypes at different ages by Laconic, a FRET-based genetic reporter. Data show mean \pm S.E.M ($n = 234, 230, 256$ and 226 cells, from left to right) based on two-way ANOVA with Tukey's multiple comparison test. **** $P < 0.0001$. **c** The percentage of ISCs with the indicated number of γH2AvD foci in aged flies (30 d) with the indicated genotypes was quantified. Data show mean \pm S.E.M ($n = 340$ and 229 cells, from left to right) based on two-way ANOVA with Tukey's multiple comparison test. * $P < 0.05$ and **** $P < 0.0001$. **d** Gut homeostasis of flies with different genotypes at different ages were monitored by the pH indicator

Bromophenol Blue. "Homeostasis", a well-defined acidic Copper cell region is flanked by basic anterior midgut and posterior midgut; "Perturbed A," the acidic region is lost and the whole gut is basic; "Perturbed B," the strongly acidic region is lost, while the rest of the gut also becomes less basic (weak blue). Representative images shown on the bottom. Data show mean \pm S.E.M ($n = 15$ guts per group) based on one-way ANOVA with Tukey's multiple comparison test. **** $P < 0.0001$. Scale bar: $1\ \text{mm}$. **e** Food intake measured using CAFÉ assay with indicated genotypes at different ages. Data show mean \pm S.E.M ($n = 12$ flies per group) based on one-way ANOVA with Tukey's multiple comparison test. **** $P < 0.0001$. **f** Representative images and quantification of deposit with indicated genotypes at different ages. Data show mean \pm S.E.M ($n = 16$ fields for each group of 15 flies) based on one-way ANOVA with Tukey's multiple comparison test. **** $P < 0.0001$. Scale bar, $1\ \text{mm}$. Each experiment was repeated for 3 times (a–f). See Supplementary Table 1 for genotypes. Source data are provided as a Source Data file.

and Supplementary Fig. 11d). These results suggested that an increase in mitochondrial Ca²⁺ promotes autophagy and delays ISCs aging by retrogradely activating Ca²⁺ release from the ER via *IP3R*.

MERCs-mediated calcium crosstalk between the ER and mitochondria involved in MitoCa²⁺-mediated autophagy in ISCs

MERCs as the physical links between the ER and mitochondria, not only serve as a ground for dynamic Ca²⁺ transfer from the ER to mitochondria⁶⁵, but also for autophagic regulation²⁸. We then tested whether MERCs is involved in the regulation of MitoCa²⁺-mediated autophagy. The physical contacts between mitochondria and ER, visualized by DsRed-targeted mitochondrial outer membrane (OMM) and KDEL-GFP labeled ER, were observed in ISCs and were enhanced by *MCU* overexpression (Supplementary Fig. 12a). To monitor MERCs in ISCs, we generated a transgenic fly expression MAMtracker-Green (MAM-GFP), a dimerization-dependent GFP (ddGFP) based reporter⁶⁶, to detect reversible changes in MERCs structure under the control of UAS-Gal4 system. When overexpressed by ISC-Gal4^{ts}, the MAM-GFP positive puncta were adjacent and partially colocalized with mitochondria and ER and autophagosomes (Supplementary Fig. 12b–e). Meanwhile, the number of MAM-GFP positive vesicles in ISCs is sensitive to genetic manipulations of known MERCs components. For instance, genetically knocking down *Grp75* (CG8542), or *Mmm1* (CG13838, a conserved component of MAM also participate in phospholipid trafficking in yeast⁶⁷) was sufficient to reduce MERCs structure, while overexpressing *Grp75* or human *VAPB* (*hVAPB*) was sufficient to increase MERCs (Fig. 5a), indicating that the MERCs structures are controlled by the conserved tethering complex in *Drosophila* and MAM-GFP is a sensitive tool to quantify the MERCs dynamics in ISCs. As expected, MitoCa²⁺ in ISCs was reduced when MERCs were genetically disrupted by *Grp75*^{RNAi} or *Mmm1*^{RNAi}, but increased when MERCs were augmented by *Grp75* or *hVAPB* overexpression (Fig. 5b and Supplementary Fig. 13a), indicating that MitoCa²⁺ levels are controlled by MERCs in ISCs. Surprisingly, increasing MitoCa²⁺ by *MCU*^{OE} promoted MERCs formation, as indicated by the number of MAM-GFP and structures observed under TEM microscope (Fig. 5c–e and Supplementary Fig. 13b). Moreover, *Itpr* knockdown profoundly suppressed the number of MAM-GFP puncta induced by *MICU1*^{RNAi}, whereas *Itpr*^{OE} was sufficient to increase MERCs (Fig. 5f and Supplementary Fig. 13c), indicating that increasing MitoCa²⁺ promoted MERCs structures by activating *IP3R*. Intriguingly, autophagy induced by MitoCa²⁺ was suppressed by *Mmm1*^{RNAi} or *Grp75*^{RNAi} (Fig. 5g, h and Supplementary Fig. 14a, b), while increasing MERCs by overexpressing *Grp75* or *hVAPB* was sufficient to promote autophagy (Fig. 5i, j and Supplementary Fig. 14c, d). Increasing MERCs by expressing an artificial tether, Tether-RFP⁶⁸, was also sufficient to increase autophagy in ISCs as indicated by Atg8a positive puncta (Fig. 5k). Taken together, these data indicated that MERCs-mediated calcium crosstalk is critical for MitoCa²⁺-mediated autophagy in ISCs.

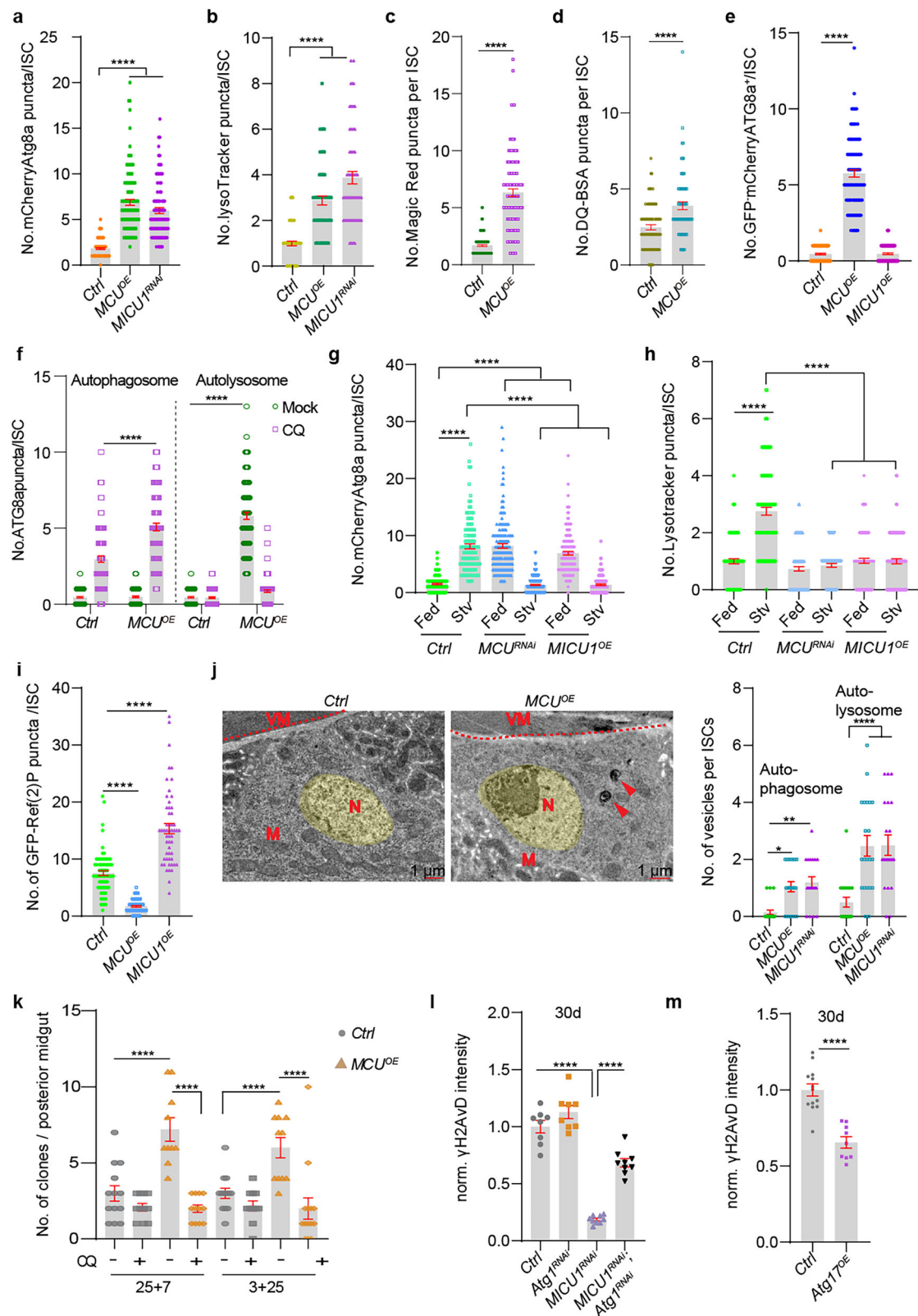
MERCs are critical for MitoCa²⁺-mediated rejuvenation of aged ISCs

We then investigated the role of MERCs in MitoCa²⁺-mediated rejuvenation of aged ISCs. Genetical upregulation of MERCs was sufficient to restore MitoCa²⁺ levels, which were reduced and insensitive to *Ecc15* infection in aged ISCs (Fig. 6a, b and Supplementary Fig. 15a, b). Furthermore, DNA damages in aged ISCs suppressed by *MCU*^{OE} were blocked by *Mmm1*^{RNAi} (Fig. 6c and Supplementary Fig. 16a). Lactate levels suppressed by *MICU1*^{RNAi} in aged ISCs were also increased by *Grp75*^{RNAi} (Fig. 6e and Supplementary Fig. 16d). Intriguingly, DNA damages, lactate levels and mis-differentiation were all restored in aged ISCs by *hVAPB*^{OE} or *Grp75*^{OE} (Fig. 6d–f and Supplementary Fig. 16b–d). Moreover, overexpression of Tether-RFP was also sufficient to reduce DNA damages in aged ISCs (Fig. 6g). Taken together, these data indicated that MERCs are critical for MitoCa²⁺-mediated rejuvenation of aged ISCs.

Breakdown of ER-mitochondria calcium crosstalk triggers ISCs aging due to defective autophagy

We then explore how MitoCa²⁺ was reduced in aged ISCs. Expression levels of components in the *MCU* complex, such as *MCU*, *MICU1* and *EMRE*, were largely unchanged in the whole intestine at different ages, as shown by RT-qPCR (Supplementary Fig. 17a). Furthermore, we found that the expression levels of some calcium-associated channels (*PMCA*, *Stim*, *Orai*, *IP3R*, *RyR*, *VDAC*, *MCU*, *MICU1* and *EMRE*) and mitochondria-ER contact tethers (*Mfn2*, *Grp75*, *VAPB*, *Mmm1*) were largely unchanged in old ISCs compared to young ISCs by RNA-seq dataset analysis (GSE157794, Supplementary Fig. 17b). Then we hypothesized that dysfunctional *IP3R* and/or MERCs lead to decreased MitoCa²⁺ in aged ISCs. Intriguingly, compared to young ISCs, despite no significant changes in ERCa²⁺ levels, ERCa²⁺ responded poorly to starvation in aged ISCs (Fig. 7a and Supplementary Fig. 17c), indicating that the activity of *IP3R* was impaired in aged ISCs. Meanwhile, the number and intensity of MAM-GFP puncta in aged ISCs were lower than those in young ISCs under both feeding and starvation conditions (Fig. 7b, c and Supplementary Fig. 17d), suggesting that the structure of MERCs was damaged in aged ISCs. These results showed that the breakdown of *IP3R*-mediated Ca²⁺ crosstalk in MERCs is critical for MitoCa²⁺ reduction in aged ISCs.

On the other hand, more p62 aggregates were observed in aged ISCs than those in young ones (Fig. 7d and Supplementary Fig. 18a, b). The number of mCherryATG8a+ puncta in aged ISCs were lower than those in young ISCs under both feeding and starvation conditions (Fig. 7e and Supplementary Fig. 18c). Notably, unlike young ISCs, starvation failed to induce an increase of mCherryATG8a+ puncta in aged ISCs (Fig. 7e and Supplementary Fig. 18c). These results showed that autophagy was impaired and autophagic machinery was less sensitive to starvation in aged ISCs. Surprisingly, although autophagic activity was reduced, *AMPK* activity (indicated by *AMPK*-SPARK



positive puncta) was actually increased in aged ISCs (Fig. 7f and Supplementary Fig. 19a), which may be due to ATP level drop caused by reduced MitoCa²⁺ in aged ISCs¹⁸. Indeed, increasing MitoCa²⁺ by overexpressing *MCU* downregulated *AMPK* activity in aged ISCs (Fig. 7f and Supplementary Fig. 19a), suggesting that autophagic failure in aged ISCs is not due to the suppression of *AMPK*.

Interestingly, increasing MitoCa²⁺ by overexpressing *MCU* was sufficient to restore *IP3R* activity, MERCs as well as autophagy in aged ISCs (Fig. 7a–e, and Supplementary Fig. 17c, d, 18a–c). Similarly, overexpression of *Itpr* or *hVAPB* was sufficient to promote autophagic activity in aged ISCs (Fig. 7g and Supplementary Fig. 19b). These results indicated that MitoCa²⁺, *IP3R* and MERCs form a positive feedback loop

Fig. 3 | Autophagy is activated by MitoCa²⁺ to delay ISC aging. a–i Quantification of the number of mCherryATG8 (a, g), lysotracker (b, h), Magic Red (c), DQ-BSA (d), autophagosomes (f), autolysosomes (e, f) and Ref(2)P-GFP (i) positive puncta in young ISCs (3 d) with indicated genotypes and conditions, respectively. Data show mean \pm S.E.M ($n = 102, 111, 91$ cells in a, $n = 71, 66, 63$ cells in b, $n = 130, 96$ cells in c, $n = 76, 68$ cells in d, $n = 100, 100, 102$ cells in e, $n = 100, 101, 100, 94$ cells in f, $n = 112, 123, 147, 163, 140, 124$ cells in g, $n = 101, 122, 120, 105, 122, 106$ cells in h and $n = 75, 70, 54$ cells in i, respectively, from left to right) based on one-way ANOVA with Tukey's multiple comparison test (a, b, e–i) and two-tailed unpaired t-test (c, d). **** $P < 0.0001$. **j** Representative images and quantification of the number of autophagosomes and/or autolysosomes in young ISCs (3 d) with indicated genotypes by TEM. VM, visceral muscles; M, mitochondria; N, nucleus. ISCs and their nucleus were circled in light yellow and typical autophagosomes or autolysosomes

were highlighted by arrowheads. Data show mean \pm S.E.M ($n = 20, 21$ and 20 cells, from left to right) based on one-way ANOVA with Tukey's multiple comparison test. * $P < 0.05$, ** $P < 0.01$ and **** $P < 0.0001$. Scale bar, $1\ \mu\text{m}$. **k** Quantification of clone numbers in the posterior midgut with indicated genotypes at different ages after treated or not with CQ for indicated time. Data show mean \pm S.E.M ($n = 13, 11, 10, 12, 13, 11, 11$ and 14 guts, from left to right) based on one-way ANOVA with Tukey's multiple comparison test. **** $P < 0.0001$. **l, m** Quantification of the intensity of anti- γH2AvD signals in ISCs of aged flies (30 d) with indicated genotypes, respectively. Data show mean \pm S.E.M ($n = 8, 8, 9, 9$ guts in l and $n = 13, 9$ guts in m) from left to right) based on one-way ANOVA with Tukey's multiple comparison test (l) and two-tailed unpaired t-test (m). **** $P < 0.0001$. Each experiment was repeated for 3 times (a–m). See Supplementary Table 1 for genotypes. Source data are provided as a Source Data file.

and the breakdown of the loop triggers ISC aging through autophagic failure, even with elevated *AMPK* activity (Fig. 7h).

Discussion

Inter-organelle communication in eukaryotic cells is spatially and temporally organized and display a transient dynamic pattern responds to pathophysiological conditions⁶⁹. MERCs, as the platforms between ER and mitochondria, actively involved in processes such as lipid trafficking, calcium crosstalk, redox homeostasis, and autophagy⁷⁰. This is corroborated by the growing body of evidence indicating that MERCs play a pivotal role in regulating the aging process and age-related diseases⁷¹. However, the mechanisms governing the number, composition, and function of MERCs, as well as the factors that disrupt their regulation during aging, remain largely unelucidated.

Here we found that subcellular Ca²⁺ homeostasis is disturbed in ISCs of aged flies: Ca²⁺ levels in the ER lumen and cytosol are maintained at higher levels, while those in the mitochondria are reduced. Compromised autophagy is a common feature of aging across diverse species⁷². In mammalian cell lines, the pro- or anti-autophagic effect of Ca²⁺ depends on the context, kinetics, amplitude or spatial extent. For example, many studies have shown that increased Cytosolic Ca²⁺ signals can activate *AMPK* through *CaMKK β* by phosphorylating pThr172^{73,74}. Activated *AMPK* then promotes autophagy by inhibiting *mTORC1* or controversially by phosphorylating *ULK1*^{75,76}. While other studies have also shown that the elevation of CytoCa²⁺ increases protein phosphatase4, which inactivates *AMPK* through dephosphorylation of pThr172⁷⁷. Reduced MitoCa²⁺ can activate *AMPK* due to energy deprivation⁷⁸. A recent study showed that a temporal decrease in ATP during mitosis would activate *AMPK*, which can activate *MCU* through phosphorylation⁷⁹. In this scenario, the *AMPK/MCU* couple helps to maintain MitoCa²⁺ level and energy status. However, we found *AMPK* activity was even increased in aged ISCs, the impaired autophagy and poor sensitivity to starvation was due to the disruption of the positive feedback loop consisting of MitoCa²⁺, MERCs via *IP3R*. Our results further indicated that *AMPK* and the MitoCa²⁺/*IP3R*/MERCs cascade are mutually required for autophagy induction. These results indicated that these two modules function in parallel to regulate autophagy induction in ISCs.

Based on the results, we propose a model in which the Ca²⁺ homeostasis in MERCs is maintained by a balance between Ca²⁺ release from the ER and Ca²⁺ uptake by mitochondria. Forced MitoCa²⁺ uptake would cause temporal drop of Ca²⁺ in MERCs, which activates *IP3R* and cause replenishment of Ca²⁺ in MERCs and forms calcium oscillations (Fig. 7h). How *IP3R* detect local Ca²⁺ drops in MERCs? *IP3Rs* are unusually large proteins, comprising tetramers of closely-related subunits, and each with about 2700 amino acid residues⁸⁰. In addition to *IP3*, Ca²⁺ was shown also to regulate *IP3R* with a biphasic concentration dependence⁸¹; modest increases in CytoCa²⁺ levels enhancing responses to *IP3*, while higher levels of CytoCa²⁺ were inhibitory for

*IP3R*⁸². It's possible that forced MitoCa²⁺ influx cause Ca²⁺ drop in the microdomain, which was sensed by *IP3R* and lead to its activation. *IP3R* activity is also regulated by its subcellular localization and post-translational modifications⁸³. For instance, *Cdk5*, a kinase localizes in MERCs, phosphorylates *IP3R1* at Ser⁴²¹ and regulates ER Ca²⁺ transfer to the mitochondria in mouse embryonic fibroblasts (MEFs)⁸⁴. Therefore, MitoCa²⁺ may also regulate *IP3R* activity through local Ca²⁺-dependent kinases or phosphatases in MERCs. Here, we found that Ca²⁺ oscillations in MERCs mediated by mitochondrial Ca²⁺ and *IP3R* form a positive feedback loop to regulate autophagy. Breakdown of this loop is a driven force for ISC aging and genetically restoring the loop is sufficient led to ISC rejuvenation through *AMPK*-independent autophagy. Given that the components are conserved, it is plausible that the MERCs-specific Ca²⁺ oscillations also function as a module for autophagy regulation in mammals. Our results provide a strategy to tackle aging and aging-related diseases.

Methods

Fly strains and reagents

Flies were cultured at 25 °C and 60% humidity with a 12 h light/dark cycle on standard yeast/molasses-based food unless otherwise indicated (recipe for 1 L food: 13.8 g agar, 22 g molasses, 75 g malt extract, 18 g dry inactivated yeast, 80 g corn flour, 10 g soy flour, 6.25 ml, propionic acid, 2 g methyl 4-hydroxybenzoate, 7.2 mL ethanol and water up to 1 L).

The following strains were obtained from the Bloomington *Drosophila* Stock Center: *w¹¹¹⁸* (BL3605), *tub::GAL80ts* (BL7108), *UAS-mCherry* (BL25774), *UAS-nls-GFP* (BL4775), *UAS-tdTomato* (BL36327), *UAS-MitoDsRed* (BL93056), *UAS-20XUAS-RcAMP1f* (BL52210), *UAS-tdTomato-P2A-GCaMP5G* (BL80079), *UAS-MCU* (BL16357), *FRT40A* (BL5759), *UAS-GFP.E2f1.1-230,UAS-mRFP1.CycB.1-266* (BL55099), *NRE::EGFP.S* (BL30727), *UAS-MitoRoGFP2.Orp1* (BL67667), *UAS-GFP-mCherry-Atg8a* (BL37749), *UAS-mCherry-ATG8a* (BL37750), *UAS-Itp^{RNAi}* (BL25937), *UAS-Itp^{RNAi}* (BL30742), *UAS-ER.GCaMP6-210* (BL83293), *UAS-Hsc70-5.FLAG.HA.V* (BL95230), *UAS-hVAPB.HA* (BL82230), *UAS-GFP-Lamp1* (BL42714), *UAS-GFP-Rab5* (BL43336), *UAS-GFP-Rab7* (BL42705), *UAS-ATG17*(BL91226), *UAS-GFP-KDEL* (BL9899), *UAS-RFP-KDEL* (BL30909), *UAS-AMPK^{CA}* (BL32110), *UAS-AMPK^{DN}* (BL32112). *UAS-MICU1^{RNAi}* (v110456), *UAS-MCU^{RNAi}* (v110781), *UAS-Hsc70-5^{RNAi}* (v47745) were obtained from Vienna *Drosophila* Stock Center (VDRC). *UAS-MICU1.ORF.3xHA* (F000962) were obtained from FlyORF. *UAS-ATG1^{RNAi}* (THU2357), *UAS-mCD8-GFP* (THJ0080), *UAS-Mmm1^{RNAi}* (THU5442) were obtained from Tsinghua University Fly Center. *esg::GAL4* was a gift from S.Hayashi, *Gbe::GAL80* from S.X.Hou, *UAS-MitoGCaMP3* from F.Kawasaki, *hsFlp;FRT40,tub::GAL80;tub::GAL4,UAS-GFP* from B.Ohlstein, *UAS-Laonic* from O.Morris, *UAS-GFP-Ref(2)P* from T.Neufeld, *TRE-RFP* from D.Bohmann, *UAS-AMPK-SPARK* from H.Huang, *UAS-GFP-ATG6*, *UAS-GFP-ATG9*, *UAS-GFP-ZFYVE1*, *UAS-Tether-RFP* from C.Tong, *UAS-mCherry-ATG13* from S.J.He. A full list of fly genotypes used in each figure panel is available in Supplementary Table 1.

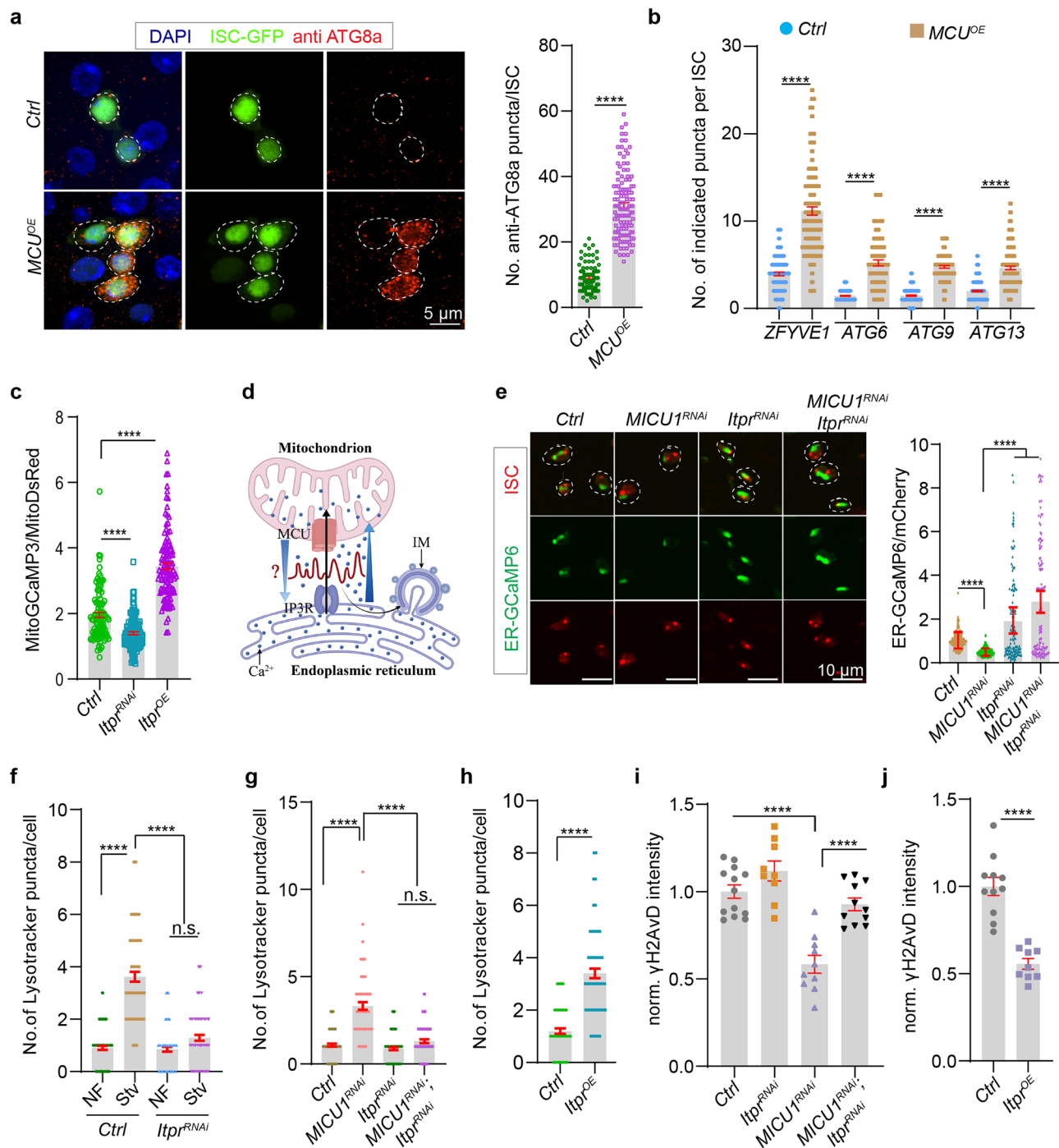
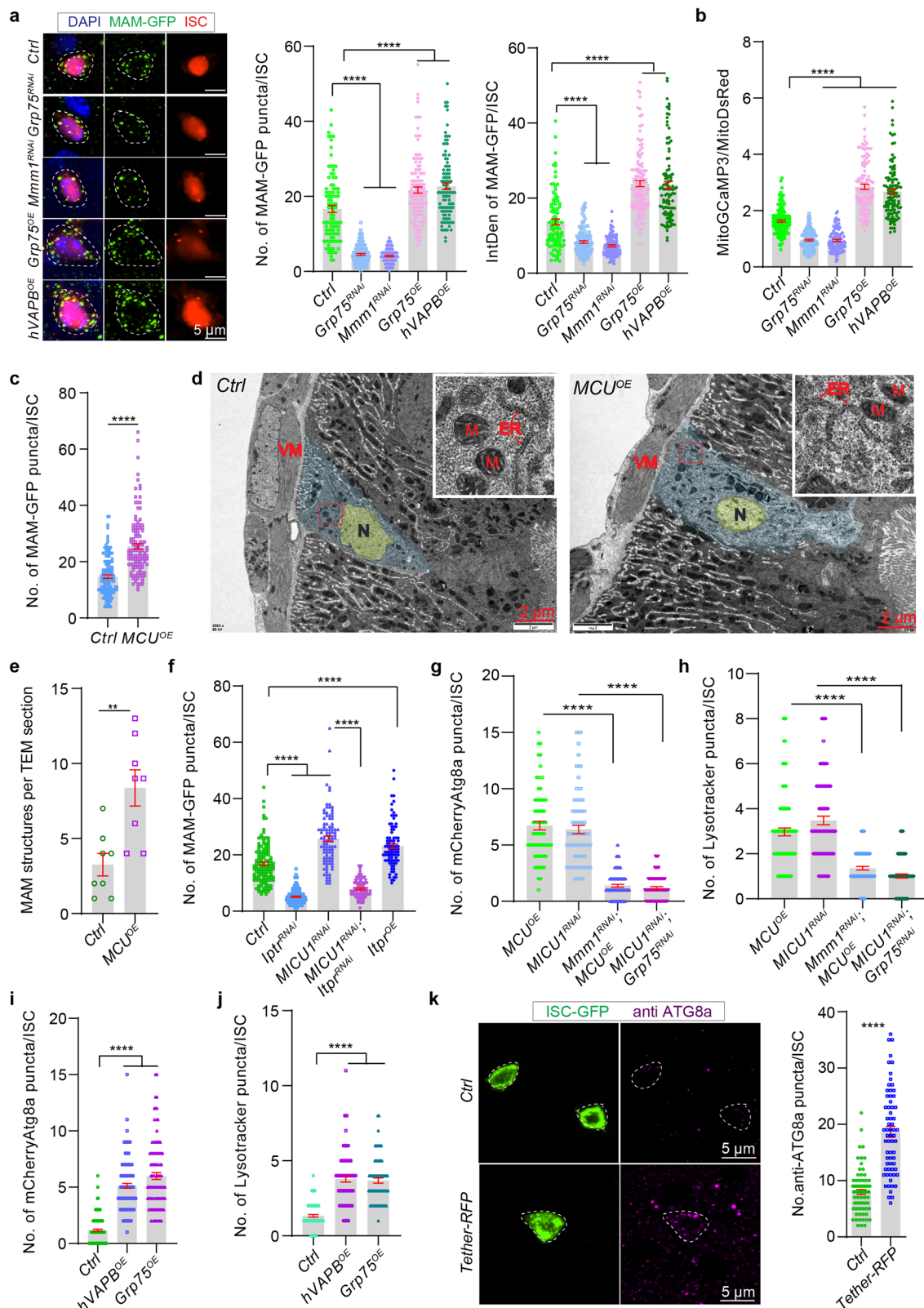


Fig. 4 | MitoCa²⁺ promotes autophagy by activating IP3R-mediated Ca²⁺ release from the ER. **a** Representative images and quantification of the number of autophagosomes in young ISCs (3 d, green) with indicated genotypes by anti-ATG8a staining (red). Data show mean \pm S.E.M. ($n = 99$ and 126 cells, from left to right) based on two-tailed unpaired t-test. **** $P < 0.0001$. Scale bars, $5 \mu\text{m}$. **b** Quantification of the number of ZFYVE1, ATG6, ATG9 and ATG13 positive puncta in young ISCs (3 d) with indicated genotypes. Data show mean \pm S.E.M. ($n = 89, 112, 109, 65, 114, 89, 132$ and 128 cells, from left to right) based on two-tailed unpaired t-test. **** $P < 0.0001$. **c** Quantification of relative MitoCa²⁺ levels in young ISCs (3 d) with indicated genotypes. Data show mean \pm S.E.M. ($n = 102, 123$ and 118 cells, from left to right) based on one-way ANOVA with Tukey's multiple comparison test. **** $P < 0.0001$. **d** Working scheme: MCU overexpression might activate IP3R (question mark) and cause Ca²⁺ release from ER, forming Ca²⁺ oscillations required for isolation membrane (IM) nucleation and autophagy initiation. **e** Representative images and quantification of relative ER-Ca²⁺ levels in young ISCs (3 d, red) with

indicated genotypes by ER-GCaMP6 (green). Typical ISC (red) was circled by dashed lines. Data show mean \pm S.E.M. ($n = 140, 115, 113$ and 127 cells, from left to right) based on one-way ANOVA with Tukey's multiple comparison test. **** $P < 0.0001$. Scale bars, $10 \mu\text{m}$. **f-h** Quantification of the number of acidic lysosomes in young ISCs (3 d) with indicated genotypes, respectively. Data show mean \pm S.E.M. ($n = 95, 82, 90, 94$ cells in **f**, $n = 95, 71, 94, 65$ cells in **g** and $n = 99, 92$ cells in **h**, from left to right) based on one-way ANOVA with Tukey's multiple comparison test (**f, g**) and two-tailed unpaired t-test (**h**). **** $P < 0.0001$. **i, j** Quantification of the intensity of anti-yH2AvD signals in aged ISCs (30 d) with indicated genotypes, respectively. Data show mean \pm S.E.M. ($n = 13, 9, 10, 11$ guts in **i** and $n = 11, 9$ guts in **j**, from left to right) based on one-way ANOVA with Tukey's multiple comparison test (**i**) and two-tailed unpaired t-test (**j**). **** $P < 0.0001$. Each experiment was repeated for 3 times (**a-c, e-j**). See Supplementary Table 1 for genotypes. Source data are provided as a Source Data file.



***Drosophila* TARGET system, aging and MARCM induction**

We used the TARGET system⁴³ and the Gene Switch system⁴⁴ for conditional expression of UAS-linked transgenes. Conditional expression in ISCs + EBs was achieved by combining ISC/EB driver *esg::Gal4* (*esg::Gal4*) with *Gal80^{TS}* (*Gal80^{TS}*), a temperature-sensitive *Gal4* inhibitor driven by a tubulin promoter (*Tub::Gal80^{TS}*). For conditional expression in only ISCs, *esg::Gal4* and *Tub::Gal80^{TS}* were combined with *Su(H)GBE-G80*, which

drives the expression of a temperature-insensitive version of *Gal80* in EBs. When using the TARGET system, flies were cultured at permissive temperature (18 °C) to avoid transgene expression before being shifted to the restrictive temperature of 29 °C for the indicated time to induce transgene expression. For experiments using our aging model, flies were kept at 18 °C for the indicated time before shifting to 29 °C for 4 days to induce transgene expression. Food was changed every 2–3 days.

Fig. 5 | MERCs-mediated calcium crosstalk between the ER and mitochondria involved in MitoCa²⁺-mediated autophagy in ISCs. **a** Representative images and quantifications of the number and intensity of MAM-GFP positive vesicles (green) in young ISCs (3 d) with indicated genotypes. Typical ISCs (red) were circled in dashed lines. Data show mean \pm S.E.M ($n = 98, 107, 104, 121$ and 107 cells, from left to right) based on one-way ANOVA with Tukey's multiple comparison test. **** $P < 0.0001$. Scale bars, $5\ \mu\text{m}$. **b** Quantification of relative MitoCa²⁺ levels in young ISCs (3 d) with indicated genotypes. Data show mean \pm S.E.M ($n = 123, 136, 104, 108$ and 111 cells, from left to right) based on one-way ANOVA with Tukey's multiple comparison test. **** $P < 0.0001$. **c** Quantification of the number of MAM-GFP positive vesicles in young ISCs (3 d) with indicated genotypes. Data show mean \pm S.E.M ($n = 129$ and 127 cells, from left to right) based on two-tailed unpaired t-test. **** $P < 0.0001$. **d, e** Representative TEM images (**d**) and quantifications (**e**) of MERCs in young ISCs (3 d) with indicated genotypes. Typical ISCs nucleus (yellow). Data show mean \pm S.E.M ($n = 8$ and 8 sections, from left to right) based on two-tailed unpaired t-test

(**e**). ** $P < 0.01$. Scale bars, $2\ \mu\text{m}$ (**d**). **f** Quantification of the number of MAM-GFP positive vesicles in young ISCs (3 d) with indicated genotypes. Data show mean \pm S.E.M ($n = 124, 114, 97, 100$ and 95 cells, from left to right) based on one-way ANOVA with Tukey's multiple comparison test. **** $P < 0.0001$. **g–j** Quantification of the number of mCherryATG8a (**g, i**) and lysotracker (**h, j**) positive puncta in young ISCs (3 d) with indicated genotypes. Data show mean \pm S.E.M ($n = 69, 75, 85, 97$ cells in **g**, $n = 93, 81, 88, 81$ cells in **h**, $n = 131, 115, 102$ cells in **i**) and $n = 90, 79, 75$ cells in **j**), from left to right) based on one-way ANOVA with Tukey's multiple comparison test. **** $P < 0.0001$. **k** Representative images and quantification of the number of autophagosomes in young ISCs (3 d) with indicated genotypes by anti-ATG8a staining (magenta). ISCs (green). Data show mean \pm S.E.M ($n = 76$ and 66 cells, from left to right) based on two-tailed unpaired t-test. **** $P < 0.0001$. Scale bars, $5\ \mu\text{m}$. Each experiment was repeated for 3 times (**a–k**). See Supplementary Table 1 for genotypes. Source data are provided as a Source Data file.

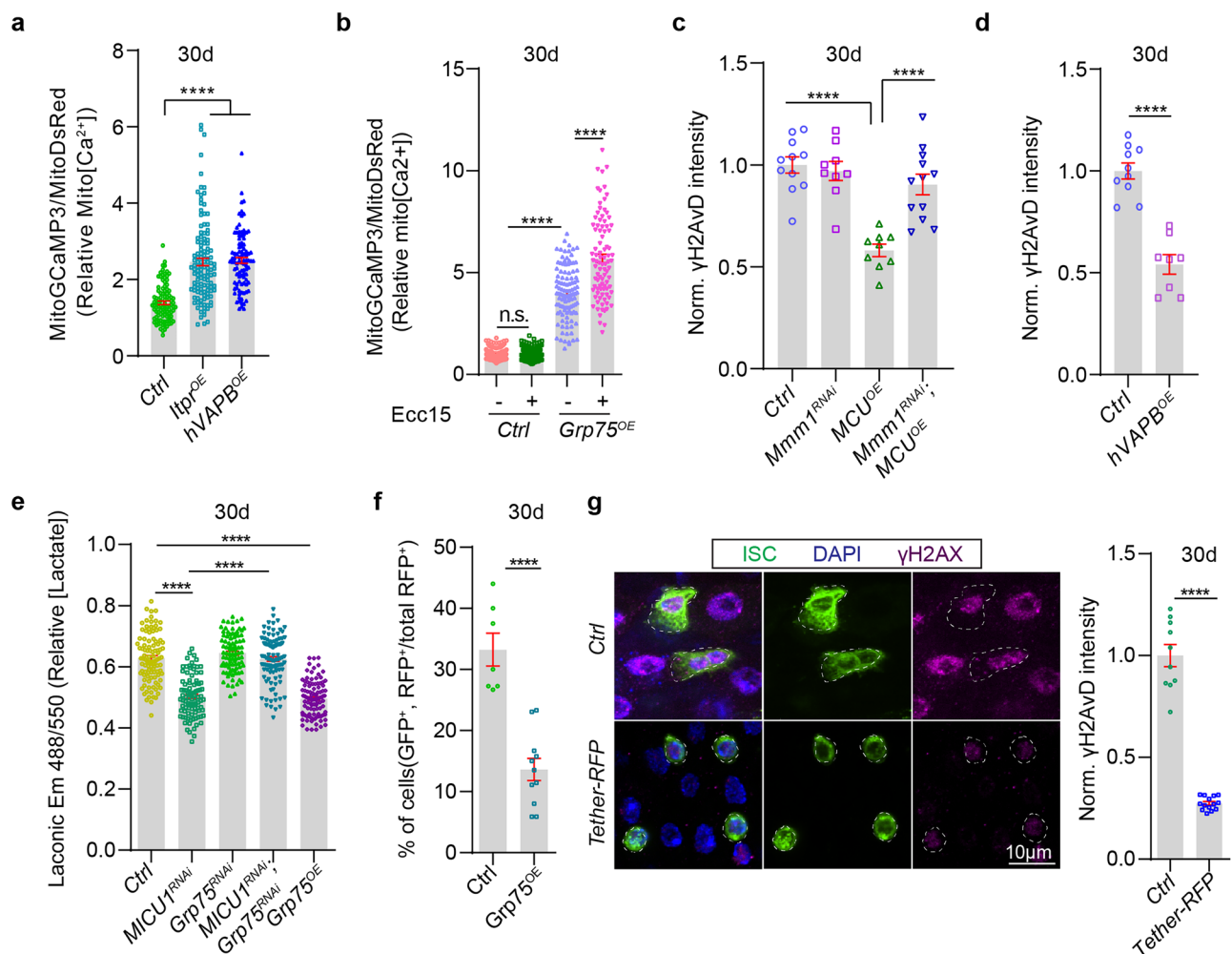
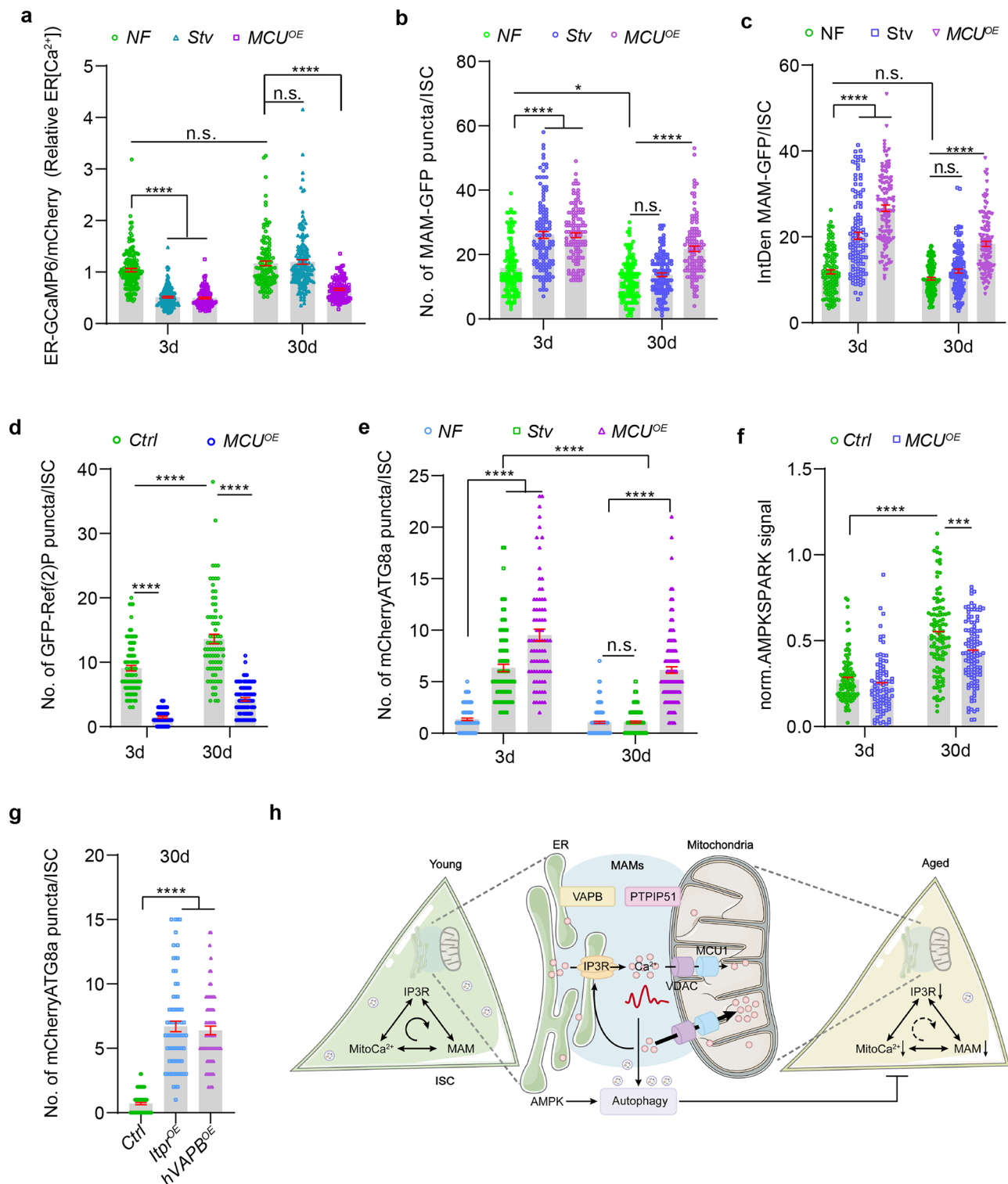


Fig. 6 | MERCs are critical for MitoCa²⁺-mediated rejuvenation of aged ISCs. **a, b** Quantification of relative MitoCa²⁺ levels in aged ISCs (30 d) with indicated genotypes exposed or not to *Ecc15* infection. Data show mean \pm S.E.M ($n = 100, 120, 95$ cells in (**a**) and $n = 137, 128, 110, 92$ cells in (**b**), from left to right) based on one-way ANOVA with Tukey's multiple comparison test. **** $P < 0.0001$. **c, d** Quantification of the intensity of γH2AvD signals in aged ISCs (30 d) with indicated genotypes. Data show mean \pm S.E.M ($n = 11, 9, 9, 12$ guts in (**c**) and $n = 10, 8$ guts in (**d**), from left to right) based on one-way ANOVA with Tukey's multiple comparison test (**c**) and two-tailed unpaired t-test (**d**). **** $P < 0.0001$. **e** Quantification of relative lactate levels in aged ISCs (30 d) with indicated genotypes by Laconic, a FRET-based genetic reporter. Data show mean \pm S.E.M ($n = 104$,

$94, 93, 102$ and 102 cells, from left to right) based on one-way ANOVA with Tukey's multiple comparison test. **** $P < 0.0001$. **f** Quantification of the number of mis-differentiation ISCs in aged flies (30 d) with indicated genotypes. Data show mean \pm S.E.M ($n = 7$ and 11 guts, from left to right) based on two-tailed unpaired t-test. **** $P < 0.0001$. **g** Representative images and quantification of the intensity of anti- γH2AvD signals (magenta) in aged ISCs (30 d) with indicated genotypes. ISCs (green), nuclei (blue). Data show mean \pm S.E.M ($n = 10$ and 14 guts, from left to right) based on two-tailed unpaired t-test. **** $P < 0.0001$. Scale bars, $10\ \mu\text{m}$. Each experiment was repeated for 3 times (**a–g**). See Supplementary Table 1 for genotypes. Source data are provided as a Source Data file.



For experiments with the 5961 GeneSwitch system, flies were raised for 3 days on normal food post eclosion and then kept for 4 days on food supplemented with RU486 at 5 mg/ml (mifepristone; Calbiochem #475838) dissolved in ethanol, or with ethanol alone (control).

For MARCM clone induction, flies were heat-shocked at 37 °C for 1 h. Following heat-shock, flies were kept at 25 °C and dissected after the indicated time. For starvation treatments, flies were transferred to fresh vials containing 5% sucrose at 29 °C for 8 h prior to dissection. In all experiments, only female posterior midgut was analyzed.

Cloning and transgenic fly generation

MAMTracker-Green (MAM-GFP) was amplified from pMAMTracker-Green, which was a gift from Koji Yamanaka, using primers Fw: GAATTCatggctattcaactcagg and Rev: CTCGAGttacttcataaaagacc. Amplified fragments were then cloned into pUAST-attB vector using EcoRI and XhoI restriction enzyme sites. For *ltp*-HA knock-in transgenic fly, the CRISPR-Cas9-based strategy was utilized to generate the homology-mediated knock-in allele of *ltp* (CG1063, the fruit fly *IP3R* homolog). Briefly, the sgRNA sequence in the CDS of CG1063 was designed by CRISPOR and cloned into the pEASY-Blunt vector. Three

Fig. 7 | The breakdown of the ER-mitochondria calcium crosstalk triggers ISC aging due to defective autophagy. **a** Quantification of relative ERCa²⁺ levels in ISCs with indicated genotypes and conditions at different ages. NF, normal food; Stv, starvation. Data show mean \pm S.E.M ($n = 150, 161, 109, 122, 159$ and 110 cells, from left to right) based on two-way ANOVA with Tukey's multiple comparison test. **** $P < 0.0001$. **b, c** Quantifications of the number and intensity of MAM-GFP positive vesicles in ISCs with indicated genotypes and conditions at different ages. Data show mean \pm S.E.M ($n = 116, 120, 121, 124, 128$ and 117 cells, from left to right) based on two-way ANOVA with Tukey's multiple comparison test. * $P < 0.05$ and **** $P < 0.0001$. **d, e** Quantifications of the number of Ref⁽²⁾P-GFP (**d**) and mCherryATG8 (**e**) positive puncta in ISCs with indicated conditions and genotypes at different ages. Data show mean \pm S.E.M ($n = 84, 61, 78, 79$ cells in (**d**) and $n = 123, 93, 78, 154, 147, 138$ cells in (**e**), from left to right) based on two-way ANOVA with Tukey's multiple comparison test. **** $P < 0.0001$. **f** Quantification of the intensity of AMPKSPARK signals in ISCs with indicated genotypes at different ages. Data

show mean \pm S.E.M ($n = 96, 93, 107$ and 110 cells, from left to right) based on two-way ANOVA with Tukey's multiple comparison test. **** $P < 0.0001$. **g** Quantification of the number of mCherryATG8a positive puncta in aged ISCs (30 d) with indicated genotypes. Data show mean \pm S.E.M ($n = 96, 74$ and 70 cells, from left to right) based on one-way ANOVA with Tukey's multiple comparison test. **** $P < 0.0001$. **h** Model schematic: in young animal ISCs, calcium oscillations in MERC were maintained by the positive cycle formed by MitoCa²⁺-IP3R-MERC. In short, increasing MitoCa²⁺ influx by *MCU* overexpressing lead to the activation of IP3R, which then promote calcium release from the ER and formed oscillations in MERC which is maintained by complexes such as *VAPB-PTPIP51* and *IP3R-VDAC* for the initiation of autophagy independent of *AMPK*. In aged ISCs, the MitoCa²⁺/IP3R/MERC cycle was disrupted, leading to impaired autophagy. Autophagosomes are indicated by double membrane vesicles. Each experiment was repeated for 3 times (**a–g**). See Supplementary Table 1 for genotypes. Source data are provided as a Source Data file.

set of primers were designed for the donor plasmid: the primer pair for the homologous arms spanning the stop codon of CG1063 and the primer for the linker plus 3xHA sequence. The sequences were then sequentially cloned into the pMDTM18-T vector. In this way, the donor plasmid was knocked into the CG1063 coding sequence just before the stop codon in frame. The sgRNA and donor construct were then microinjected into fly (BL78781) embryos. Positive transgenic lines were verified by sequencing.

The primers for sgRNA CG1063 sg-F 5' tacagactcactgaacggcGT TTTAGAGCTAGAAATAGC 3' and CG1063 sg-R 5' gccgtttcagtgagctgtaCGACGTTAAATTGAAAATAGG 3'. The primers for donors CG1063 Lpart-FCGACGATATCTCTAGctaatataactgactttcagttactttaccact, CG1063 Lpart-RAGTCCGGActgaaacggcaggaggc, CG1063 linker+3x HA-F gtttcagTCCGGACTCAGATCTGGCAGC, CG1063 linker+3x HA-R cagactcaAGCGTAGTCTGGGACGTCG, CG1063 Rpart-F CTACGCTgag tctgtaagaataagaataataactaattttggcac and CG1063 Rpart-R ATGACCA TGATTACGCCCTCAATCCACTCCACGC. The transformation injection was performed in the Core Facility of *Drosophila* Resource and Technology, CAS (Shanghai).

Ecc15 infection and Chloroquine treatment

Bacteria *Ecc15* were cultured overnight at 30 °C in LB medium. A concentrated bacterial pellet ($A_{600\text{nm}}$ of ~200), which was centrifuged from 1-ml overnight culture media, was resuspended 1:1 with 5% sucrose to yield an *Ecc15* infection solution. Flies were starved at 29 °C for 2 h and then transferred to fresh vials covered with a filter paper (WhatmanTM) and either 150 μL of *Ecc15* infection solution or 5% sucrose (mock) solution. Flies were infected for 16 h before dissection for Ca²⁺ imaging.

As previously described⁸⁵, for CQ treatment (Chloroquine diphosphate salt solid, #C6628, Sigma-Aldrich), tubes containing food supplemented with 100 μM CQ were used. Briefly, for MARCM clones, flies were starved at 25 °C for 2 h to synchronize feeding and transferred to tubes containing food supplemented with 100 μM CQ for 2 days before heat-shock. Following heat-shock, flies were kept at 25 °C and transferred to tubes containing supplemented 100 μM CQ every 2 days and dissected after the indicated time.

Bromophenol blue assay

The bromophenol blue assay was used to detect the pH change in the midgut as previously described⁴⁵. Briefly, 100 μL of 2% Bromophenol blue sodium (Sigma, B5525) was added to the food surface and several holes were poked to allow the Bromophenol blue solution completely absorbed by the food. Images were taken immediately after 16 h.

Cafe assay and fly excretion measurement

For Café assay, a 5 μL capillary containing liquid food (10% yeast, 10% sucrose, and blue dye) was inserted into a cotton plug of 6 cm long vial, and 1 cm high 1% agar was at the vial bottom to keep the moisture. The

food intake was recorded every 12 h and the capillary was changed every 24 h. For fly excretion measurement, flies were dry starved for 2 h and put into Bromophenol blue vial food for 24 h, and then the deposits on the vial wall were imaged and quantified.

RNA isolation and quantitative real-time PCR

RNA was isolated from guts of 15 flies using TriZol reagent (#15596026 Life technologies). Around 20 μg RNA then were reversely transcribed using 5X All-In-One RT Mastermix With AccuRT Kit (#G592, Applied Biological Materials) according to the manufacturer's instructions. All of the reactions were performed in triplicate in a CFX96TM Real-Time System (Bio-Rad Laboratories). The following primers pairs were used: *MCU*, 5'-GTCTCGCCCTGCGTTGG-3' and 5'-CGAAGCTTCTGTGCTGCTG-3'; *MICU1*, 5'-GTGGCCATGGTCAATCTTTC-3' and 5'-TTGTTGCTGAGTTGGTTGTCA-3'; *EMRE*, 5'-ACATGTCCAGCGTGTACTTTC-3' and 5'-GGTATGACGGCACAGAAGATG-3'; *Rp49*, 5'-GCCGCTCAAGGGACAGTATCTG-3' and 5'-AACGCGGTTCTGCATGAG-3'. Expression was normalized with *Rp49* and quantification was performed using the comparative CT method.

Transmission electron microscopy

Guts were dissected in PBS, fixed with 2.5% glutaraldehyde, and washed three times with 0.1M phosphate buffer at 4 °C, post-fixed with 1.0% OsO₄ for 1 h at 4 °C, washed with phosphate buffer, dehydrated in ethanol, and embedded in Spurr resin. Thick section was stained with Toluidine blue and ultra-thin sections of the embedded guts were double-stained with uranyl acetate and lead citrate and examined with a JEM1400 transmission electron microscope (TEM).

Immunostaining and florescence microscopy

Female fly midguts were dissected in PBS and fixed for 20 min at room temperature in 4% formaldehyde. After fixation, the samples were washed with PBS containing 0.5% bovine serum albumin and 0.1% Triton X-100 (PBST) for 1 h. Appropriate primary antibodies were added to the samples and incubated at 4 °C overnight. Midguts were washed and then incubated with secondary antibodies for 4 h at room temperature. Samples were mounted in Mounting Medium (#S2100, Solarbio). The following antibodies or dyes were used: rabbit anti-Histone H2AvD pS137 (1:200; #600-401-914, Rockland); rabbit anti-Ref⁽²⁾P (1:500; #ab178440, Abcam); rabbit anti-Atg8a (GABARAP⁵⁷) (1:500; #13733S Cell Signaling Technology); rabbit anti-HA (1:250; #3724 T, Cell Signaling); rabbit anti-cleaved Caspase 3 (1:100; #Y407558, Applied Biological Materials); rabbit anti-phospho-4EBP1 (1:200; #2855S, Cell Signaling); rabbit anti-GFP (1:500; #PABG1, Chromotek); Alexa-488-conjugated donkey anti-rabbit secondary antibody (1:1000; #A21206, Molecular Probes); Goat- α -rabbit-IgG(H + L)-Cy3 secondary antibody (1:1000; #A10520, Molecular Probes); Goat- α -rabbit-IgG(H + L)-Cy5 secondary antibody (1:1000; #A10523, Molecular Probes); and Hoechst 33342 (0.1 $\mu\text{g mL}^{-1}$, 6 min incubation;

#H1399, Invitrogen). All images were taken on a Zeiss Axio Imager M2 fluorescence microscope equipped with a 40× Plan-Apochromat oil-immersion objective lens (Zeiss) or an Olympus IXplore SpinSR confocal microscope equipped with a 100×1.5 NA oil-immersion objective lens (Olympus) and processed using Adobe Photoshop, Illustrator and Image J.

LipidTOX, LysoTracker, propidium iodide, Magic Red and DQ-BSA staining

LipidTox staining was performed as previously described¹⁸⁶. In brief, fixed guts were washed 3 times for 5 min in PBST, then directly stained with LipidTOX™ solution (1:200, # H34476, Invitrogen) diluted in PBST, mounted in Mounting Medium with Hoechst and analyzed on a confocal microscope.

For LysoTracker staining, guts were dissected in AHLS and incubated in AHLS containing 0.5 μM LysoTracker Red (#C1046, Beyotime) for 5 min at room temperature. They were then mounted similarly to all other live-imaging experiments and imaged immediately by a two-photon laser microscope.

For propidium iodide staining, guts were dissected in PBS and then stained in 1.5 μM PI (#P1304MP, Invitrogen) for 15 min at room temperature. The guts were then fixed for 20 min in 4% formaldehyde, washed three times in PBS, mounted in Mounting Medium with Hoechst and analyzed on a confocal microscope.

For Magic Red and DQ-BSA staining, guts were dissected in AHLS and incubated in AHLS containing Magic Red (1:250, #ICT-941, Immunochemistry) or DQ-BSA (4 μg ml⁻¹, #D12051, Invitrogen) for 10 min at room temperature. They were then mounted similarly to all other live-imaging experiments and imaged immediately by a two-photon laser microscope.

Ex vivo *Drosophila* intestine imaging setup

Flies were dissected in Adult Hemolymph-like Saline (AHLS) culture media containing 2 mM CaCl₂, 5 mM KCl, 5 mM HEPES, 8.2 mM MgCl₂, 108 mM NaCl, 4 mM NaHCO₃, 1 mM NaH₂PO₄, 5 mM Trehalose and 10 mM Sucrose. Guts were rapidly transferred to a microscope slide with thin adhesive spacers (#GBL654008, Sigma-Aldrich), embedded in 1% low melting agarose (in AHLS) and submerged in AHLS. All live-imaging experiments were imaged using an Olympus FVMPE-RS two-photon microscope equipped with two lasers for fluorescence excitation. Only the middle posterior midgut region (region R4) was analyzed.

Image acquisition and quantifications

For Cyto[Ca²⁺], Mito[Ca²⁺] and ER[Ca²⁺] imaging experiments except Fig. 1B, identical sized z stacks covering a single layer of the *Drosophila* epithelium were imaged using an Olympus FVMPE-RS two-photon microscope equipped with two lasers for fluorescence excitation. An InSight X3-OL laser (Spectra-Physics) tuned to 530–550 nm was used to excite TdTomato/DsRed/mCherry, and a MaiTai eHPDS-OL laser (Spectra-Physics) tuned to 488 nm was used to excite GCaMP3/5/6. The laser beams were focused using a 25× 1.05 NA water-immersion objective lens (Olympus). GCaMP3/5/6 emission was captured at 495–540 nm and TdTomato/DsRed/mCherry emission at 575–645 nm. For Cyto[Ca²⁺] and Mito[Ca²⁺] imaging experiments in Fig. 1b, images were taken on a Zeiss Axio Imager M2 fluorescence microscope equipped with an apotome. The laser beams were focused using a 40× Plan-Apochromat oil-immersion objective lens (Zeiss).

For the ratiometric MitoRoGFP2_Orp1 biosensor, experiments were performed based previous publications^{18,87}. Freshly dissected midgut tissues were incubated with 20 mM NEM (N-ethyl maleimide, #E387, Sigma-Aldrich) (in AHLS) for 10 min before imaging. Probe fluorescence was excited sequentially using the 405 nm and 488 nm laser lines and emission was detected at 495–540 nm.

For Laconic FRET imaging experiments, following excitation using the 440 nm laser line, emission was sequentially detected at 460–500 nm and 520–560 nm.

For AMPK-SPARK imaging experiments, EGFP was excited at 488 nm and emission was detected at 495–540 nm, mCherry was excited at 545 nm and emission was detected at 575–645 nm.

All quantifications were done manually using FIJI (NIH ImageJ) software. When sensors were expressed using *esg::G4* in the absence of *Su(H)GBE::G80ts*, regions of interest (ROIs) were manually drawn so as to only segment smaller cells that likely represent ISCs and early-stage EBs. Larger *esg::G4* positive cells, which are probably late-stage EBs that are soon approaching differentiation into ECs, were excluded from analysis.

For MARCM clone analysis, the clone formation and maintenance capacity of ISCs was measured by quantifying the number of MARCM clones containing at least 3 cells in the posterior midgut.

For ISC cell cycle analysis using the Fucci system, the nucleus of GFP, RFP, GFP/RFP and non-fluorescent labeled ISC indicated cell residing in G1, S, G2 and G0 phase, respectively. The number of different fluorochrome-tagged nuclei was manually quantified across the whole posterior midgut.

For ISC differentiation analysis, ISCs and EB cells were labeled with mCherry and GFP, respectively. The mis-differentiation of ISCs was measured by quantified the percentage of ISCs labeled with mCherry and GFP.

For γH2AvD measurements, γH2AvD foci per nuclei of ISCs was counted manually. Mean intensity quantifications were made in individual ISCs of GFP channels normalized to nearby background.

For p-4EBP1, Ref(2)P, TRE-RFP and GFP-MAM measurements, mean intensity quantifications were made in individual ISCs of GFP or mCherry channels normalized to nearby background.

For mCherry-ATG8a, LysoTracker, GFP-Ref(2)P, GFP-ZFYVE1, GFP-ATG6, GFP-ATG9, mCherry-ATG13 and GFP-MAM puncta measurements, number quantifications were counted in individual ISCs of GFP or mCherry channels.

For Cyto[Ca²⁺], Mito[Ca²⁺] and ER[Ca²⁺] measurements, mean intensity quantifications were made in the ROIs of RCAMP1, MitoG-CaMP3, GCaMP5/TdTomato, MitoGCaMP3/TdTomato, MitoGCaMP3/MitoDsRed or ERGCaMP6/mCherry channels.

For ratiometric measurements of MitoRoGFP2_Orp1, mean intensity quantifications were made in the ROIs of both 405 nm and 488 nm excitation channels.

For ratiometric FRET measurements of Laconic, mean intensity quantifications were then made in the ROIs of both the 460–500 nm and 520–560 nm emission channels.

For ratiometric measurements of AMPKSPARK, mean intensity quantifications were made in the ROIs of EGFP/mCherry channels.

For Magic Red and DQ-BSA staining, the number and intensity of puncta were quantified in ISCs which labeled by GFP.

Statistical analysis

Statistical analysis is performed using GraphPad Prism 8. Data derived from different genetic backgrounds or different conditions were compared using Student's two-tailed unpaired t-test, one-way ANOVA followed by Tukey's multiple comparison test, two-way ANOVA followed by Tukey's multiple comparison test as indicated in the figure legends. All data were presented as mean ± SEM. The significance was set at *P* < 0.05. **P* < 0.05, ***P* < 0.01, ****P* < 0.001, *****P* < 0.0001, ns = non-significant (*P* > 0.05). All experiments were performed in biological triplicates.

Reporting summary

Further information on research design is available in the Nature Portfolio Reporting Summary linked to this article.

Data availability

All materials are available from the corresponding author upon request. Source data are provided with this paper.

References

- Micchelli, C. A. & Perrimon, N. Evidence that stem cells reside in the adult *Drosophila* midgut epithelium. *Nature* **439**, 475–479 (2006).
- Ohlstein, B. & Spradling, A. The adult *Drosophila* posterior midgut is maintained by pluripotent stem cells. *Nature* **439**, 470–474 (2006).
- Jiang, H. & Edgar, B. A. Intestinal stem cells in the adult *Drosophila* midgut. *Exp. Cell Res* **317**, 2780–2788 (2011).
- Biteau, B., Hochmuth, C. E. & Jasper, H. JNK activity in somatic stem cells causes loss of tissue homeostasis in the aging *Drosophila* gut. *Cell Stem Cell* **3**, 442–455 (2008).
- Biteau, B., Karpac, J., Hwangbo, D. & Jasper, H. Regulation of *Drosophila* lifespan by JNK signaling. *Exp. Gerontol.* **46**, 349–354 (2011).
- Sammels, E. et al. Polycystin-2 activation by inositol 1,4,5-trisphosphate-induced Ca^{2+} release requires its direct association with the inositol 1,4,5-trisphosphate receptor in a signaling microdomain. *J. Biol. Chem.* **285**, 18794–18805 (2010).
- Patergnani, S. et al. Various aspects of calcium signaling in the regulation of apoptosis, autophagy, cell proliferation, and cancer. *Int. J. Mol. Sci.* **21**, 8323 (2020).
- Deng, H., Gerencser, A. A. & Jasper, H. Signal integration by Ca^{2+} regulates intestinal stem-cell activity. *Nature* **528**, 212–217 (2015).
- Loncke, J. et al. Balancing ER-Mitochondrial Ca^{2+} Fluxes in Health and Disease. *Trends Cell Biol.* **31**, 598–612 (2021).
- Patron, M. et al. MICU1 and MICU2 finely tune the mitochondrial Ca^{2+} uniporter by exerting opposite effects on MCU activity. *Mol. Cell* **53**, 726–737 (2014).
- Fan, M. et al. Structure and mechanism of the mitochondrial Ca^{2+} uniporter holocomplex. *Nature* **582**, 129–133 (2020).
- Young, M. P. et al. Metabolic adaptation to the chronic loss of Ca^{2+} signaling induced by KO of IP(3) receptors or the mitochondrial Ca^{2+} uniporter. *J. Biol. Chem.* **298**, 101436 (2022).
- Herzig, S. & Shaw, R. J. AMPK: guardian of metabolism and mitochondrial homeostasis. *Nat. Rev. Mol. Cell Biol.* **19**, 121–135 (2018).
- Garcia, D. & Shaw, R. J. AMPK: Mechanisms of Cellular Energy Sensing and Restoration of Metabolic Balance. *Mol. Cell* **66**, 789–800 (2017).
- Ahumada-Castro, U. et al. MTOR-independent autophagy induced by interrupted endoplasmic reticulum-mitochondrial Ca^{2+} communication: a dead end in cancer cells. *Autophagy* **15**, 358–361 (2019).
- Cardenas, C. et al. Essential regulation of cell bioenergetics by constitutive InsP3 receptor Ca^{2+} transfer to mitochondria. *Cell* **142**, 270–283 (2010).
- Engedal, N. et al. Modulation of intracellular calcium homeostasis blocks autophagosome formation. *Autophagy* **9**, 1475–1490 (2013).
- Morris, O., Deng, H., Tam, C. & Jasper, H. Warburg-like Metabolic Reprogramming in Aging Intestinal Stem Cells Contributes to Tissue Hyperplasia. *Cell Rep.* **33**, 108423 (2020).
- He, L., Si, G., Huang, J., Samuel, A. D. T. & Perrimon, N. Mechanical regulation of stem-cell differentiation by the stretch-activated Piezo channel. *Nature* **555**, 103–106 (2018).
- Rizzuto, R. et al. Close contacts with the endoplasmic reticulum as determinants of mitochondrial Ca^{2+} responses. *Science* **280**, 1763–1766 (1998).
- Ziegler, D. V., Martin, N. & Bernard, D. Cellular senescence links mitochondria-ER contacts and aging. *Commun. Biol.* **4**, 1323 (2021).
- Csordas, G., Weaver, D. & Hajnoczky, G. Endoplasmic reticulum-mitochondrial contactology: structure and signaling functions. *Trends Cell Biol.* **28**, 523–540 (2018).
- Hirabayashi, Y. et al. ER-mitochondria tethering by PDZD8 regulates Ca^{2+} dynamics in mammalian neurons. *Science* **358**, 623–630 (2017).
- Yang, M. et al. Mitochondria-associated er membranes - the origin site of autophagy. *Front Cell Dev. Biol.* **8**, 595 (2020).
- Feng, Y., He, D., Yao, Z. & Klionsky, D. J. The machinery of macroautophagy. *Cell Res* **24**, 24–41 (2014).
- Zhao, Y. G. & Zhang, H. Formation and maturation of autophagosomes in higher eukaryotes: a social network. *Curr. Opin. Cell Biol.* **53**, 29–36 (2018).
- Diao, J. et al. ATG14 promotes membrane tethering and fusion of autophagosomes to endolysosomes. *Nature* **520**, 563–566 (2015).
- Hamasaki, M. et al. Autophagosomes form at ER-mitochondria contact sites. *Nature* **495**, 389–393 (2013).
- Zheng, Q. et al. Calcium transients on the ER surface trigger liquid-liquid phase separation of FIP200 to specify autophagosome initiation sites. *Cell* **185**, 4082–4098 e4022 (2022).
- Leidal, A. M., Levine, B. & Debnath, J. Autophagy and the cell biology of age-related disease. *Nat. Cell Biol.* **20**, 1338–1348 (2018).
- Garcia-Prat, L. et al. Autophagy maintains stemness by preventing senescence. *Nature* **529**, 37–42 (2016).
- Foerster, E. G. et al. How autophagy controls the intestinal epithelial barrier. *Autophagy* **18**, 86–103 (2022).
- Zhang, P. et al. An SH3PX1-Dependent Endocytosis-Autophagy Network Restrains Intestinal Stem Cell Proliferation by Counteracting EGFR-ERK Signaling. *Dev. Cell* **49**, 574–589 e575 (2019).
- Nagy, P., Sandor, G. O. & Juhasz, G. Autophagy maintains stem cells and intestinal homeostasis in *Drosophila*. *Sci. Rep.* **8**, 4644 (2018).
- Ulgherait, M., Rana, A., Rera, M., Graniel, J. & Walker, D. W. AMPK modulates tissue and organismal aging in a non-cell-autonomous manner. *Cell Rep.* **8**, 1767–1780 (2014).
- Wang, M. C., Bohmann, D. & Jasper, H. JNK extends life span and limits growth by antagonizing cellular and organism-wide responses to insulin signaling. *Cell* **121**, 115–125 (2005).
- Haller, S. et al. mTORC1 Activation during Repeated Regeneration Impairs Somatic Stem Cell Maintenance. *Cell Stem Cell* **21**, 806–818 e805 (2017).
- Choi, S. et al. Mitochondrial calcium uniporter in *Drosophila* transfers calcium between the endoplasmic reticulum and mitochondria in oxidative stress-induced cell death. *J. Biol. Chem.* **292**, 14473–14485 (2017).
- Tufi, R. et al. Comprehensive Genetic Characterization of Mitochondrial Ca^{2+} Uniporter Components Reveals Their Different Physiological Requirements In Vivo. *Cell Rep.* **27**, 1541–1550 e1545 (2019).
- Zacharioudaki, E. & Bray, S. J. Tools and methods for studying Notch signaling in *Drosophila melanogaster*. *Methods* **68**, 173–182 (2014).
- Lee, T. & Luo, L. Mosaic analysis with a repressible cell marker for studies of gene function in neuronal morphogenesis. *Neuron* **22**, 451–461 (1999).
- Zielke, N. et al. Fly-FUCCI: a versatile tool for studying cell proliferation in complex tissues. *Cell Rep.* **7**, 588–598 (2014).
- McGuire, S. E., Mao, Z. & Davis, R. L. Spatiotemporal gene expression targeting with the TARGET and gene-switch systems in *Drosophila*. *Sci. STKE* **2004**, pl6 (2004).
- Rodriguez-Fernandez, I. A., Tauc, H. M. & Jasper, H. Hallmarks of aging *Drosophila* intestinal stem cells. *Mech. Ageing Dev.* **190**, 11285 (2020).
- Cognigni, P., Bailey, A. P. & Miguel-Aliaga, I. Enteric neurons and systemic signals couple nutritional and reproductive status with intestinal homeostasis. *Cell Metab.* **13**, 92–104 (2011).
- Li, H., Qi, Y. & Jasper, H. Preventing age-related decline of gut compartmentalization limits microbiota dysbiosis and extends lifespan. *Cell Host Microbe* **19**, 240–253 (2016).

47. Tsujimoto, Y. Apoptosis and necrosis: intracellular ATP level as a determinant for cell death modes. *Cell Death Differ.* **4**, 429–434 (1997).
48. Singh, S. R. et al. The lipolysis pathway sustains normal and transformed stem cells in adult *Drosophila*. *Nature* **538**, 109–113 (2016).
49. Frost, L. S., Dhingra, A., Reyes-Reveles, J. & Boesze-Battaglia, K. The use of DQ-BSA to monitor the turnover of autophagy-associated cargo. *Methods Enzymol.* **587**, 43–54 (2017).
50. Hamalisto, S. et al. Spatially and temporally defined lysosomal leakage facilitates mitotic chromosome segregation. *Nat. Commun.* **11**, 229 (2020).
51. Mauvezin, C., Ayala, C., Braden, C. R., Kim, J. & Neufeld, T. P. Assays to monitor autophagy in *Drosophila*. *Methods* **68**, 134–139 (2014).
52. Mauthe, M. et al. Chloroquine inhibits autophagic flux by decreasing autophagosome-lysosome fusion. *Autophagy* **14**, 1435–1455 (2018).
53. Klionsky, D. J. et al. Guidelines for the use and interpretation of assays for monitoring autophagy (3rd edition). *Autophagy* **12**, 1–222 (2016).
54. Aparicio, R., Rana, A. & Walker, D. W. Upregulation of the Autophagy Adaptor p62/SQSTM1 Prolongs Health and Lifespan in Middle-Aged *Drosophila*. *Cell Rep.* **28**, 1029–1040 e1025 (2019).
55. Fujioaka, Y. et al. Structural basis of starvation-induced assembly of the autophagy initiation complex. *Nat. Struct. Mol. Biol.* **21**, 513–521 (2014).
56. Jipa, A. et al. Analysis of *Drosophila* Atg8 proteins reveals multiple lipidation-independent roles. *Autophagy* **17**, 2565–2575 (2021).
57. Barekat, A. et al. Using *Drosophila* as an integrated model to study mild repetitive traumatic brain injury. *Sci. Rep.* **6**, 25252 (2016).
58. Yi, S., Wang, L., Ho, M. S. & Zhang, S. The autophagy protein Atg9 functions in glia and contributes to parkinsonian symptoms in a *Drosophila* model of Parkinson's disease. *Neural Regen. Res* **19**, 1150–1155 (2024).
59. Li, Y. et al. Metabolic control of progenitor cell propagation during *Drosophila* tracheal remodeling. *Nat. Commun.* **13**, 2817 (2022).
60. Insolera, R., Lorincz, P., Wishnie, A. J., Juhasz, G. & Collins, C. A. Mitochondrial fission, integrity and completion of mitophagy require separable functions of Vps13D in *Drosophila* neurons. *PLoS Genet* **17**, e1009731 (2021).
61. Wu, H., Wang, M. C. & Bohmann, D. JNK protects *Drosophila* from oxidative stress by transcriptionally activating autophagy. *Mech. Dev.* **126**, 624–637 (2009).
62. Yin, Y. et al. The CRTG-CREB axis functions as a transcriptional sensor to protect against proteotoxic stress in *Drosophila*. *Cell Death Dis.* **13**, 688 (2022).
63. Hasan, G. & Rosbash, M. *Drosophila* homologs of two mammalian intracellular Ca(2+)-release channels: identification and expression patterns of the inositol 1,4,5-trisphosphate and the ryanodine receptor genes. *Development* **116**, 967–975 (1992).
64. Oliva, M. K., Perez-Moreno, J. J., O'Shaughnessy, J., Wardill, T. J. & O'Kane, C. J. Endoplasmic reticulum lumenal indicators in *Drosophila* reveal effects of HSP-related mutations on endoplasmic reticulum calcium dynamics. *Front Neurosci.* **14**, 816 (2020).
65. Hayashi, T., Rizzuto, R., Hajnoczky, G. & Su, T. P. MAM: more than just a housekeeper. *Trends Cell Biol.* **19**, 81–88 (2009).
66. Sakai, S., Watanabe, S., Komine, O., Sobue, A. & Yamanaka, K. Novel reporters of mitochondria-associated membranes (MAM), MAM-trackers, demonstrate MAM disruption as a common pathological feature in amyotrophic lateral sclerosis. *FASEB J.* **35**, e21688 (2021).
67. Jeong, H., Park, J., Jun, Y. & Lee, C. Crystal structures of Mmm1 and Mdm12-Mmm1 reveal mechanistic insight into phospholipid trafficking at ER-mitochondria contact sites. *Proc. Natl Acad. Sci. USA* **114**, E9502–E9511 (2017).
68. Xu, L. et al. Miga-mediated endoplasmic reticulum-mitochondria contact sites regulate neuronal homeostasis. *Elife* **9**, e56584 (2020).
69. Petkovic, M., O'Brien, C. E. & Jan, Y. N. Interorganelle communication, aging, and neurodegeneration. *Genes Dev.* **35**, 449–469 (2021).
70. Simmen, T. & Herrera-Cruz, M. S. Plastic mitochondria-endoplasmic reticulum (ER) contacts use chaperones and tethers to mould their structure and signaling. *Curr. Opin. Cell Biol.* **53**, 61–69 (2018).
71. Janikiewicz, J. et al. Mitochondria-associated membranes in aging and senescence: structure, function, and dynamics. *Cell Death Dis.* **9**, 332 (2018).
72. Aman, Y. et al. Autophagy in healthy aging and disease. *Nat. Aging* **1**, 634–650 (2021).
73. Hawley, S. A. et al. Calmodulin-dependent protein kinase kinase-beta is an alternative upstream kinase for AMP-activated protein kinase. *Cell Metab.* **2**, 9–19 (2005).
74. Woods, A. et al. Ca2+/calmodulin-dependent protein kinase kinase-beta acts upstream of AMP-activated protein kinase in mammalian cells. *Cell Metab.* **2**, 21–33 (2005).
75. Hardie, D. G. AMP-activated/SNF1 protein kinases: conserved guardians of cellular energy. *Nat. Rev. Mol. Cell Biol.* **8**, 774–785 (2007).
76. Park, J. M., Lee, D. H. & Kim, D. H. Redefining the role of AMPK in autophagy and the energy stress response. *Nat. Commun.* **14**, 2994 (2023).
77. Tomar, D. et al. Blockade of MCU-mediated Ca(2+) uptake perturbs lipid metabolism via PP4-dependent AMPK dephosphorylation. *Cell Rep.* **26**, 3709–3725 e3707 (2019).
78. Rizzuto, R., De Stefani, D., Raffaello, A. & Mammucari, C. Mitochondria as sensors and regulators of calcium signalling. *Nat. Rev. Mol. Cell Biol.* **13**, 566–578 (2012).
79. Zhao, H. et al. AMPK-mediated activation of MCU stimulates mitochondrial Ca(2+) entry to promote mitotic progression. *Nat. Cell Biol.* **21**, 476–486 (2019).
80. Taylor, C. W. & Tovey, S. C. I. P. 3) receptors: toward understanding their activation. *Cold Spring Harb. Perspect. Biol.* **2**, a004010 (2010).
81. Jean, T. & Klee, C. B. Calcium modulation of inositol 1,4,5-trisphosphate-induced calcium release from neuroblastoma x glioma hybrid (NG108-15) microsomes. *J. Biol. Chem.* **261**, 16414–16420 (1986).
82. Marshall, I. C. & Taylor, C. W. Biphasic effects of cytosolic Ca2+ on Ins(1,4,5)P3-stimulated Ca2+ mobilization in hepatocytes. *J. Biol. Chem.* **268**, 13214–13220 (1993).
83. Prole, D. L. & Taylor, C. W. Structure and Function of IP(3) Receptors. *Cold Spring Harb Perspect Biol.* **11**, a035063 (2019).
84. NavaneethaKrishnan, S., Law, V., Lee, J., Rosales, J. L. & Lee, K. Y. Cdk5 regulates IP3R1-mediated Ca(2+) dynamics and Ca(2+)-mediated cell proliferation. *Cell Mol. Life Sci.* **79**, 495 (2022).
85. Blazquez-Bernal, A., Fernandez-Costa, J. M., Bargiela, A. & Artero, R. Inhibition of autophagy rescues muscle atrophy in a LGMD2 *Drosophila* model. *FASEB J.* **35**, e21914 (2021).
86. Ma, P. et al. Mifepristone (RU486) inhibits dietary lipid digestion by antagonizing the role of glucocorticoid receptor on lipase transcription. *iScience* **24**, 102507 (2021).
87. Albrecht, S. C., Barata, A. G., Grosshans, J., Teleman, A. A. & Dick, T. P. In vivo mapping of hydrogen peroxide and oxidized glutathione reveals chemical and regional specificity of redox homeostasis. *Cell Metab.* **14**, 819–829 (2011).

Acknowledgements

We thank Bloomington *Drosophila* Stock Center, Vienna *Drosophila* Stock Center, Tsinghua Fly Center and Dr. Margaret S Ho, Dr. Hai Huang, Dr. Chao Tong, Dr. Heinrich Jasper for stocks and reagents. We thank Dr. Hong Zhang for helpful discussions. This work was supported by a National Key Research and Development Project [2018YFA0107100],

National Natural Science Foundation of China [grant no. 31871371 and 32071147] to H.D.

Author contributions

Y. Z. and H. D. conceived and designed the study. H.D. prepared the first draft of the paper. Y.Z., P.M., S.W., S.C. contributed to the experimental work. Y.Z. conducted the statistical analysis of the data.

Competing interests

The authors declare no competing interests.

Additional information

Supplementary information The online version contains supplementary material available at <https://doi.org/10.1038/s41467-025-60196-4>.

Correspondence and requests for materials should be addressed to Hansong Deng.

Peer review information *Nature Communications* thanks Dorian Ziegler, Margret Bülow, and the other, anonymous, reviewer(s) for their contribution to the peer review of this work. A peer review file is available.

Reprints and permissions information is available at <http://www.nature.com/reprints>

Publisher's note Springer Nature remains neutral with regard to jurisdictional claims in published maps and institutional affiliations.

Open Access This article is licensed under a Creative Commons Attribution-NonCommercial-NoDerivatives 4.0 International License, which permits any non-commercial use, sharing, distribution and reproduction in any medium or format, as long as you give appropriate credit to the original author(s) and the source, provide a link to the Creative Commons licence, and indicate if you modified the licensed material. You do not have permission under this licence to share adapted material derived from this article or parts of it. The images or other third party material in this article are included in the article's Creative Commons licence, unless indicated otherwise in a credit line to the material. If material is not included in the article's Creative Commons licence and your intended use is not permitted by statutory regulation or exceeds the permitted use, you will need to obtain permission directly from the copyright holder. To view a copy of this licence, visit <http://creativecommons.org/licenses/by-nc-nd/4.0/>.

© The Author(s) 2025